Science Advances
AAAS

Supplementary Materials for

Complex 3D microfluidic architectures formed by mechanically guided compressive buckling

Haiwen Luan, Qihui Zhang, Tzu-Li Liu, Xueju Wang, Shiwei Zhao, Heling Wang, Shenglian Yao, Yeguang Xue, Jean Won Kwak, Wubin Bai, Yameng Xu, Mengdi Han, Kan Li, Zhengwei Li, Xinchen Ni, Jilong Ye, Dongwhi Choi, Quansan Yang, Jae-Hwan Kim, Shuo Li, Shulin Chen, Changsheng Wu, Di Lu, Jan-Kai Chang, Zhaoqian Xie, Yonggang Huang*, John A. Rogers*

*Corresponding author. Email: y-huang@northwestern.edu (Y.H.); jrogers@northwestern.edu (J.A.R.)

Published 20 October 2021, *Sci. Adv.* **7**, eabj3686 (2021)
DOI: 10.1126/sciadv.abj3686

The PDF file includes:

- Supplementary Text
- Legends for movies S1 to S6
- Figs. S1 to S41

Other Supplementary Material for this manuscript includes the following:

- Movies S1 to S6

Supplementary Text

Supplementary Note 1 – Selected considerations in mechanics to facilitate the formation of an open-mesh spheroid geometry.

The open-mesh spheroid geometry consists of a dome-shaped top part and a basin-shaped bottom part. In the top part, the shape (e.g., overall radius) of the dome is dominated by the degree of compression provided by structural elements, including the longitudinal and lateral ribbons (both labeled in fig. S1, top). The lengths of these ribbons dictate the height of the 3D geometry. The stiffnesses (e.g., bending, and torsional) of these load-bearing structural elements constrain the resilient tendency of the dome. The resilient force from the dome transfers onto the pair of lateral ribbons along their transverse direction. Figure S4 highlights considerations in the shapes and dimensions of the lateral ribbons; these features have large transverse stiffnesses. The results indicate that wide, straight 3D ribbons have enhanced transverse stiffnesses compared to those of curved ribbons (candidates 3 & 4 in fig. S4) for the formation of a dome-shaped microvascular network. The two longitudinal ribbons on both ends reinforce the lateral ribbons in constraining the dome; their lengths are engineered to optimize the constraining effect.

The bottom part of the double-layer 3D network includes a pair of relatively wide support ribbons (labeled in fig. S1, bottom) to facilitate the formation of a basin shape. The wider support ribbon (with larger bending stiffness) results in stronger compression from the side, while a local decrease in the width (by 56%, shown in the dashed ellipse in fig. S1, bottom) just beside the microchannel network renders a relatively compliant section such that larger bending of the ribbon occurs locally for an improved wall geometry of the basin.

Supplementary Note 2 – Relationships between applied strain $\varepsilon_{\mathrm{appl}}$, prestrain $\varepsilon_{\mathrm{pre}}$, and compressive strain $\varepsilon_{\mathrm{compr}}$.

In the experimental setup, an elastomer substrate is mounted on a stretcher through four rectangular clamps (shown in orange in fig. S10A) for biaxial stretching (or through two opposite clamps for uniaxial stretching).

Figure S10 presents FEA results of biaxially stretching a silicone elastomer substrate (diameter 140 mm, thickness 1.5 mm). Figure S10A shows the configurations (top view) before and after $\varepsilon_{\mathrm{appl}}$ = 100% applied strain. The applied strain to the elastomer substrate $\varepsilon_{\mathrm{appl}}$ along each axis is defined as the change in the ratio of the net distance between opposite clamps (measured between inner edges of the clamps). For instance, in fig. S10A, the net distance in the undeformed configuration ($\varepsilon_{\mathrm{appl}} = 0$) is L_0 = 72 mm, and it becomes L = 144 mm. The change in the ratio of 100% gives the magnitude of the applied strain along both *x*- and *y*- axes. In this work, equal-biaxial stretching was typically used, $\varepsilon_{\mathrm{appl}} = \varepsilon_{\mathrm{appl}\text{-}x} = \varepsilon_{\mathrm{appl}\text{-}y}$.

As illustrated in fig. S10B, the strain contour on the elastomer substrate upon biaxial stretching is not perfectly uniform. The prestretched strain $\varepsilon_{\mathrm{pre}}$, or prestrain for short, on the substrate is the local stretching strain due to the overall prestretching of elastomer substrate, and is highly location dependent. The deformed configurations of three circular regions (all concentric with the elastomer substrate) of different diameters on a same substrate appear on the right panel of fig. S10B. The central region in the substrate shows a relatively uniform strain distribution, and the uniformity deteriorates as the diameter of the region increases. The prestrain $\varepsilon_{\mathrm{pre}}$ is practically expressed as the average stretching strain along the *x*-/*y*-axis within a specific region for the purpose of 3D assembly. Figure S10 (C and D) shows the dependence of the local strain (the maximum principal strain in (c), and the prestrain $\varepsilon_{\mathrm{pre}}$ in (d)) in the central regions (with $d_0 < 10$ mm, 10 mm $\leq d_0 < 20$ mm, and 20 mm $\leq d_0 < 30$ mm, respectively) with respect to the overall applied strain $\varepsilon_{\mathrm{appl}}$.

As the 2D microfluidic precursor structures are transferred to a local region on the prestretched elastomer substrate for compressive buckling, the magnitude and direction of prestrain $\varepsilon_{\mathrm{pre}}$ affect the final 3D geometries. In this work, the prestrain $\varepsilon_{\mathrm{pre}}$ for assembling a 3D microfluidic structure is approximately the average stretching strain within the substrate region where the 2D precursor structure mounts.

Upon gradual release of the prestretched substrate, the elastomer substrate tends to shrink back to its undeformed shape, simultaneously compressing the 2D precursor structure through the bonding sites. When the stiffness of the elastomer substrate is sufficiently large compared to the microfluidic structure, the elastomer substrate can fully recover its original shape, with negligible constraints from the microfluidic structure, upon full release of the prestrain. Under the assumption of a sufficiently stiff elastomer substrate, the compressive strain $\varepsilon_{\mathrm{compr}}$ on the microfluidic structure is related to the prestrain $\varepsilon_{\mathrm{pre}}$ on the elastomer substrate through a geometric relation, $\varepsilon_{\mathrm{compr}} = \varepsilon_{\mathrm{pre}}/(1 + \varepsilon_{\mathrm{pre}})$ for full prestrain release, and $\varepsilon_{\mathrm{compr}} = (\varepsilon_{\mathrm{pre2}} - \varepsilon_{\mathrm{pre1}})/(1 + \varepsilon_{\mathrm{pre2}})$ for partial prestrain release ($\varepsilon_{\mathrm{pre2}} > \varepsilon_{\mathrm{pre1}}$).

Supplementary Note 3 – Prevention of collapse of microchannels.

During compressive buckling, the cross-sectional dimensions of the microchannels can change, and the degree of these changes depends on parameters outlined in Fig. 2c and figs. S12–S15. In these FEA studies, both the contribution of the hydraulic pressure and the adhesion between the top and bottom walls of the microchannels are omitted for simplicity.

To avoid collapse of the microchannels, (i) the dimensions of the microchannels are designed such that less than ~30% of channel height changes at the centerline (which shows the largest change in the cross-section) during 3D assembly (without considering hydraulic pressure and adhesion between the top and bottom channel walls), and (ii) the deformed (usually decreased) channel height at the centerline is used as the effective channel height as a check for channel collapse, per the procedure outlined in *(56)*.

Alternatively, for a more accurate comparison, one can compare the difference between the increased elastic strain energy ($\Delta U_{\mathrm{deform}}$) and released adhesion energy ($A\gamma$, with a negative sign in front denoting released energy) based on a 3D microfluidic structure,

$$\Delta U_{\mathrm{total}} = \Delta U_{\mathrm{deform}} - A\gamma,$$

where A stands for the total contact area between the top and bottom wall surfaces of the microchannels due to adhesion, and γ stands for the work of adhesion. If the total energy change ($\Delta U_{\mathrm{total}}$) is negative, then adhesion between the top and bottom wall surfaces of microchannels occurs in favor of the energy state; otherwise, no adhesion occurs.

Supplementary Movies

Movie S1. 3D assembly process (FEA) of the double-layer 3D dome microvascular network presented in Fig. 1.

Movie S2. 3D assembly process (FEA) of four 3D microvascular networks presented in Fig. 2 (A and B).

Movie S3. 3D assembly (A) and fluid injection processes (B) (experiment) of a bell-shaped microvascular network presented in Fig. 2B.

Movie S4. 3D assembly process (FEA) of two biomimetic 3D microvascular networks presented in Fig. 4.

Movie S5. Thermal imaging animation of the hybrid microfluidic-electronic system during injection of hot water.

Movie S6. Comparison of infrared thermal imaging and temperature mapping by 4-by-4 array of thermistors of the hybrid microfluidic-electronic system during injection of hot water.

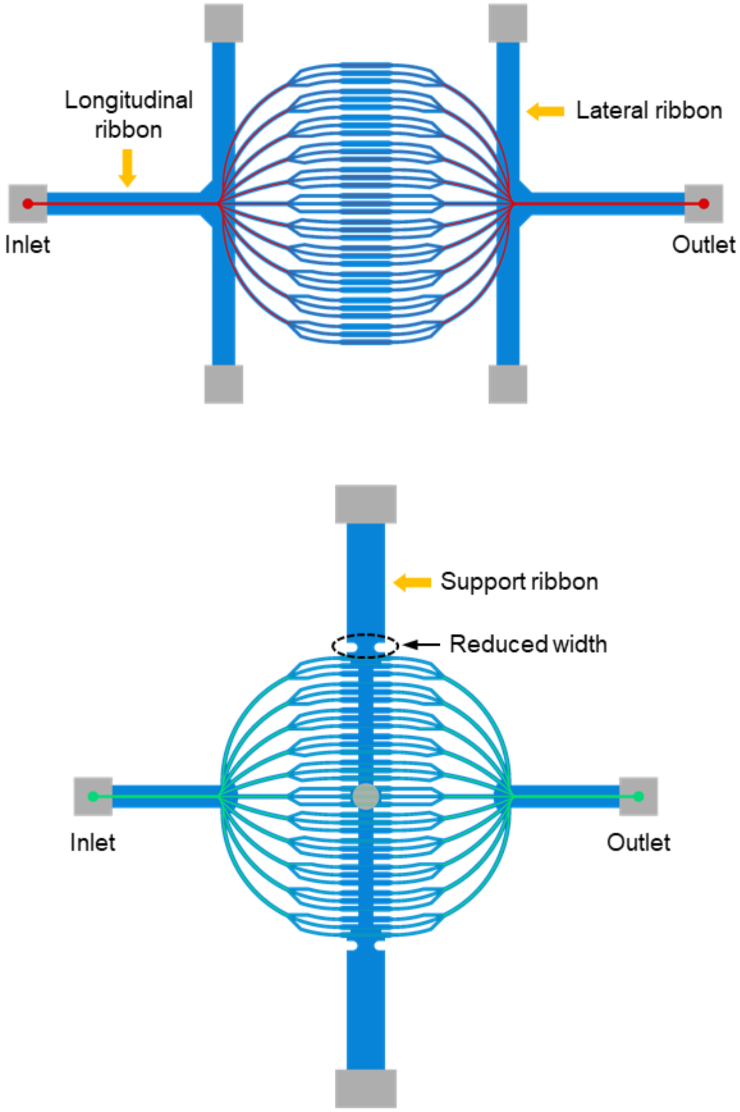

Fig. S1. 2D microfluidic precursors of the double-layer 3D dome microchannel network presented in Fig. 1.

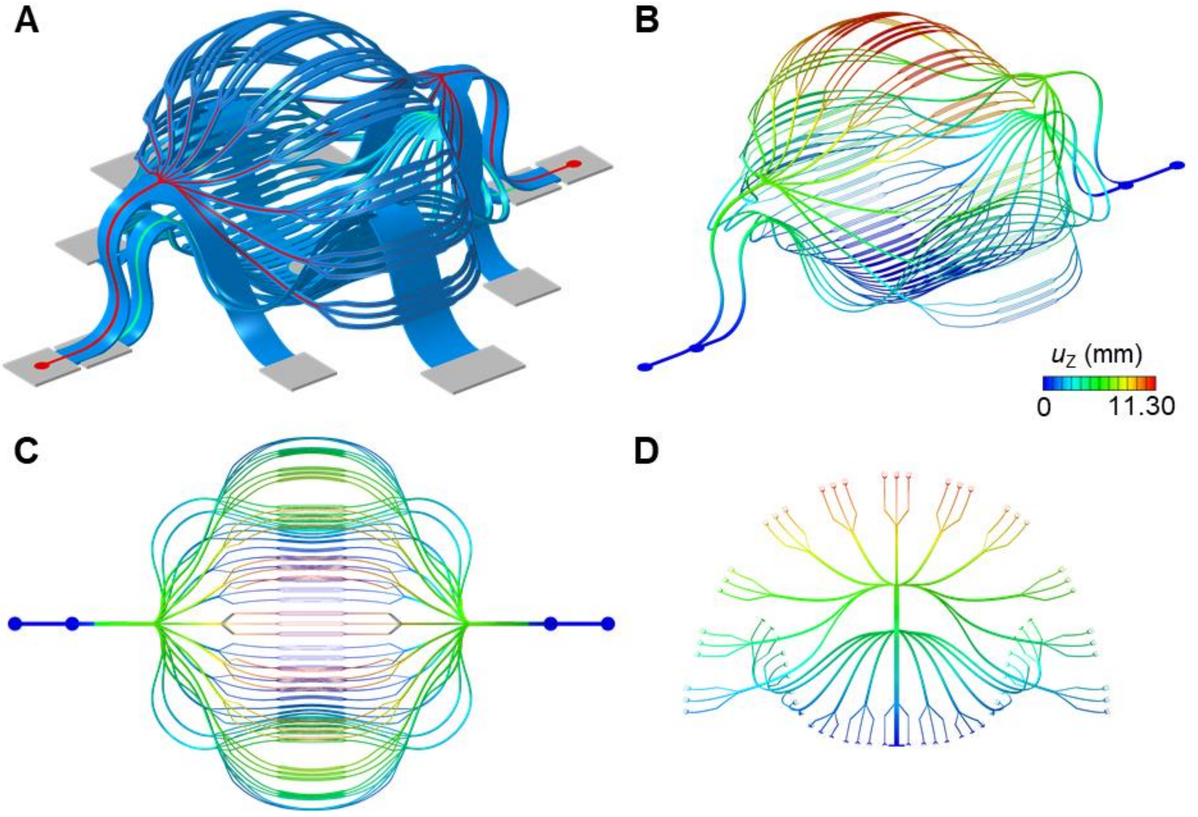

Fig. S2. A double-layer 3D biomimetic microvascular network comparable to a real, basic vascular network. The narrowest microfluidic channel branches are 10 μm wide. (A) The 3D shape of the double-layer 3D network. (B–D) The 3D microchannels in the double-layer 3D microvascular network, from 3D view (b), top view (C) and side view (D), respectively. The color bar range for (B–D) is the same.

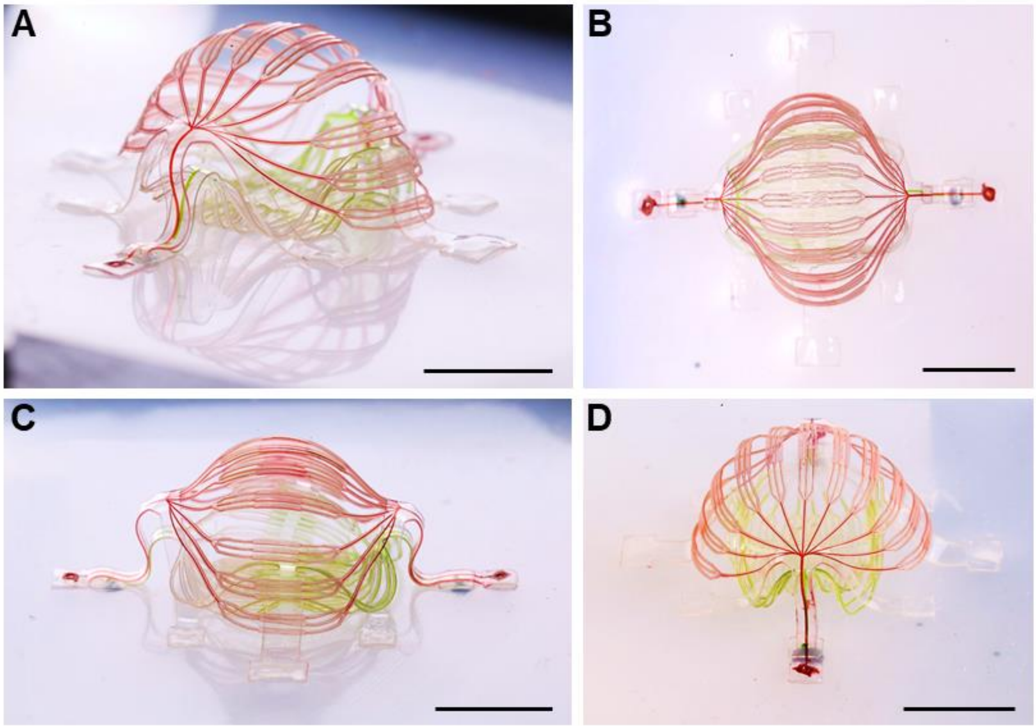

Fig. S3. Additional optical images of the double-layer 3D dome microchannel network presented in Fig. 1. Images taken from (A) 3D view, (B) top view, (C) approximately side view, and (D) approximately front view, respectively. Scale bars, 8 mm.

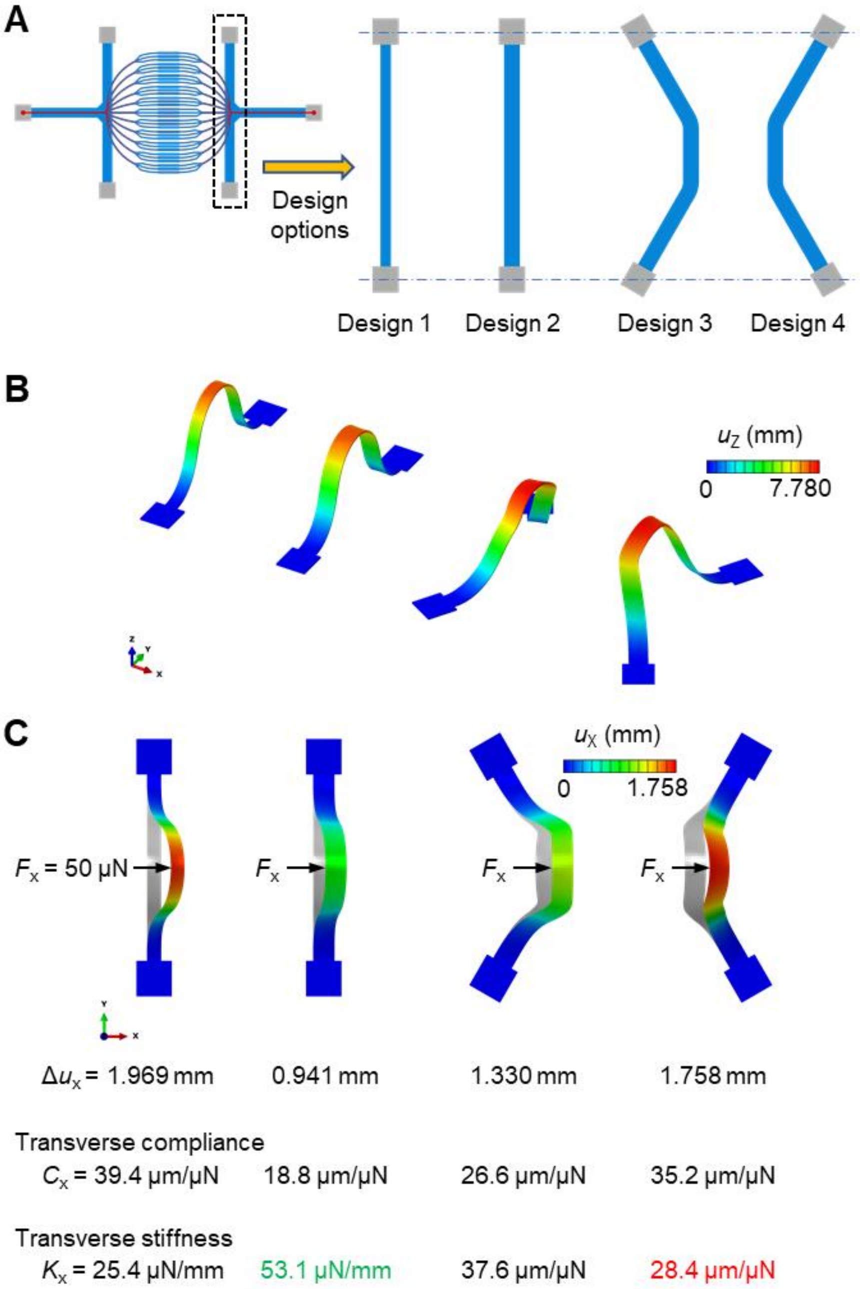

Fig. S4. Pursuit of a desirable design of lateral ribbon with enough transverse stiffness to render the dome shape in the top-layer microchannel network presented in Fig. 1 with aid of FEA. (A) Four design candidates with different shapes and dimensions. (B) The 3D geometries of the design candidates at 50% prestrain. (C) Lateral displacements and associated transverse compliances/stiffnesses of the four designs under a same transverse load of 50 μN, respectively. A wide, straight 3D ribbon provides a sufficiently large transverse stiffness.

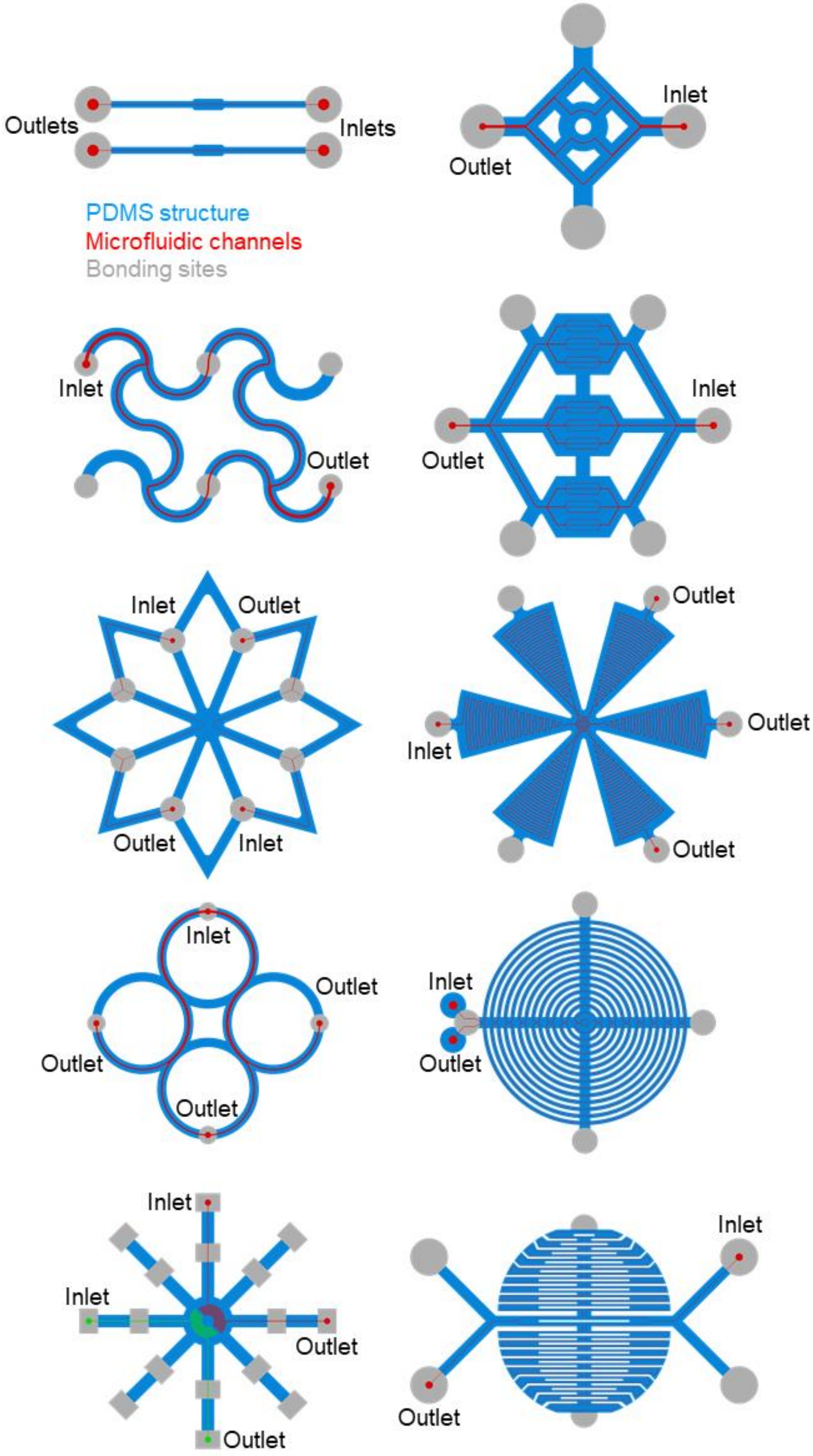

Fig. S5. 2D microfluidic precursors of the various design examples in Fig. 2 (A and B).

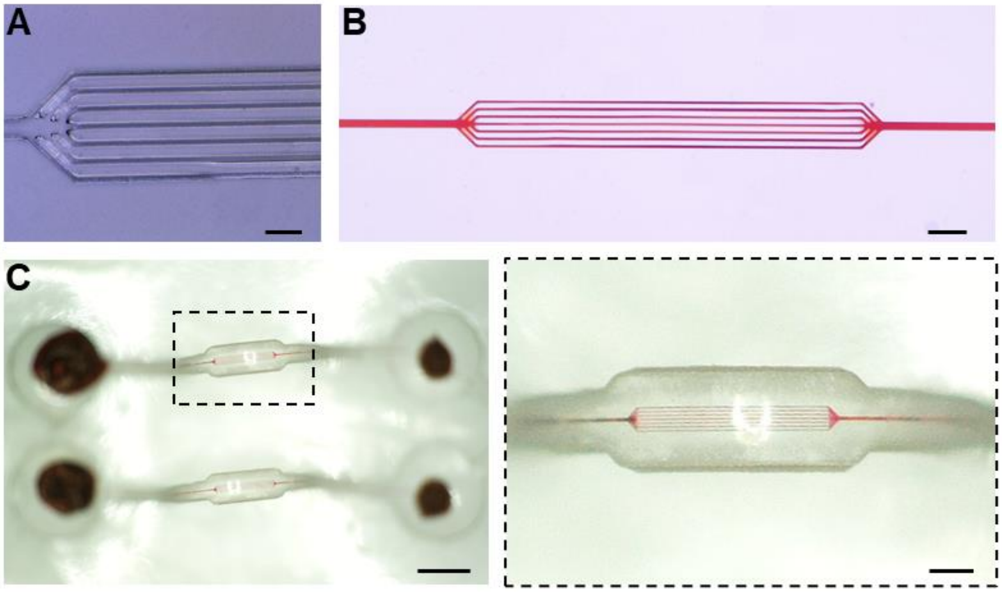

Fig. S6. Detailed optical images of the 3D microfluidic ribbon structure with a collection of 7 parallel 4-µm wide microchannels at 20 µm center-to-center spacing. (A) Empty microchannels embedded in PDMS. (B) 2D microchannels filled with water dyed in red. (C) 3D microfluidic networks from top view and a magnified image of the dashed rectangular region on the left. Scale bars, 40 µm in (A), 100 µm in (B), 800 µm in (C, left), and 200 µm in (C, right).

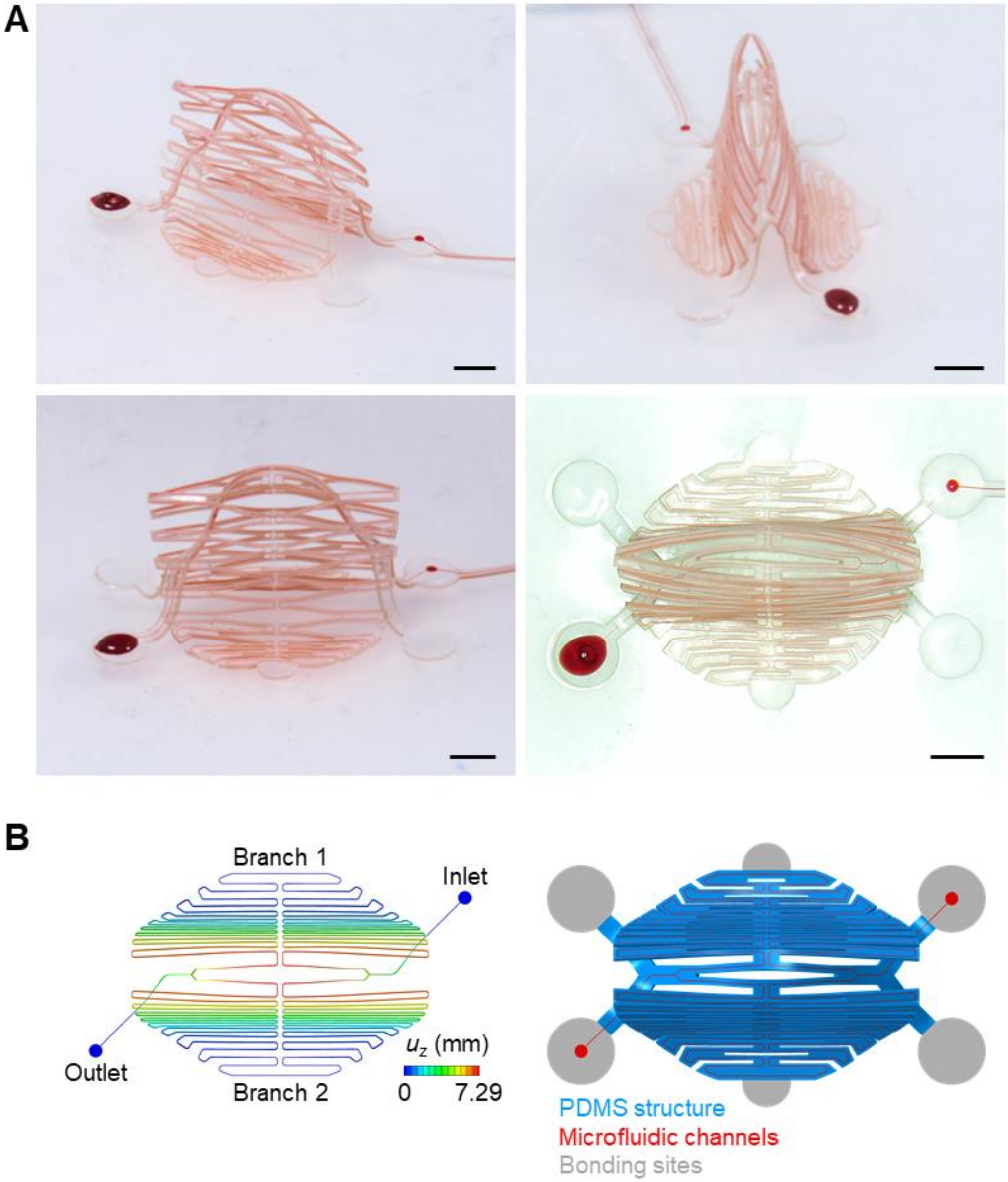

Fig. S7. A complex, kirigami-inspired 3D microvascular structure with a double-branch microchannel. The biaxial prestrain for popping up the 3D structure is 50%. Microchannel dimensions, 25 μm wide and 50 μm high. (A) Additional optical images of the kirigami-inspired 3D microchannel network. (B) FEA predictions of the postbuckling configurations of the 3D microvascular network and the 3D structure, respectively, from top view. Scale bars, 2 mm.

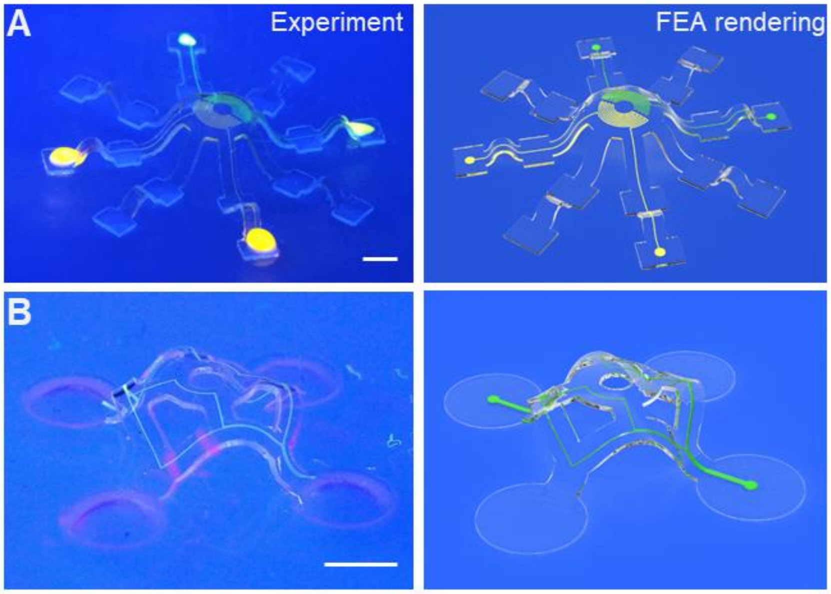

Fig. S8. Fluorescence images and FEA renderings of two 3D microvascular structures. (A) A 3D “octopus” microvascular structure. (B) A 3D microvascular structure with ribbons supporting a hollow disk. (The structures were not fabricated in the same batch as those in Fig. 2.) Microchannel dimensions, 25~100 μm wide and 50 μm high. PDMS thickness, 160 μm. Florescent dyes: Rhodamine 6G and Alexa Fluor 594 Dextran. Scale bars, 1 mm.

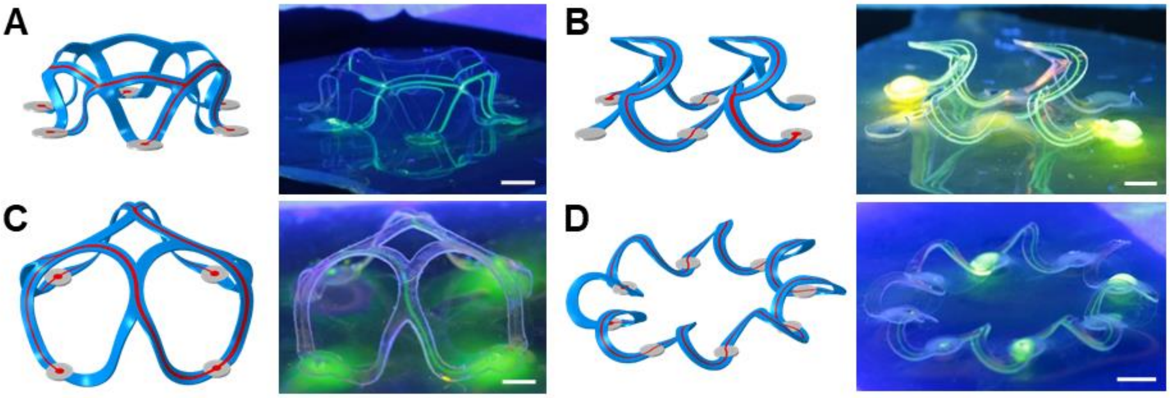

Fig. S9. FEA predictions and fluorescence images of four 3D microvascular structures. (The structures were not fabricated in the same batch as those in Fig. 2.) The biaxial prestrain for popping up the four 3D structures is 50%. In the FEA results, microfluidic channels are displayed in red, bonding sites in gray, main structures made of PDMS in blue. Microchannel dimensions, 25~200 μm wide and 50 μm high. PDMS thickness, 200 μm. The Microchannels are filled with fluorescent dye. Scale bars, 1 mm.

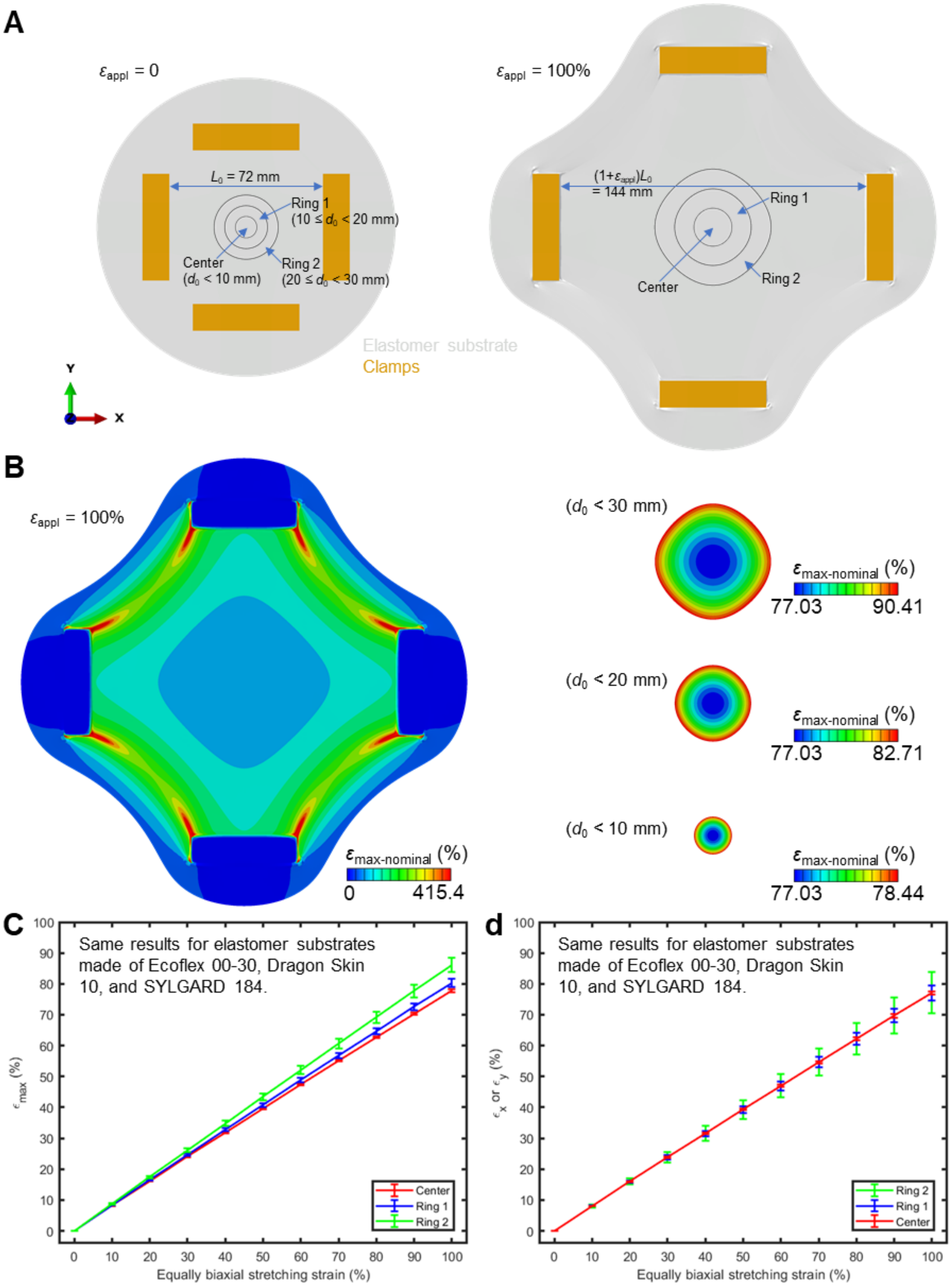

Fig. S10. Strain distribution on an elastomer substrate under biaxial stretching on a mechanical stretcher. (A) The configurations of a substrate before and after ε_{appl} = 100% biaxial stretching from top view. (B) The strain contour (showing nominal maximum principal strain) on a substrate at ε_{appl} = 100% stretching. (C, D) The average strain (nominal maximum principal strain in (C), and nominal normal strain in (D)) in three regions near the substrate center at different applied strains.

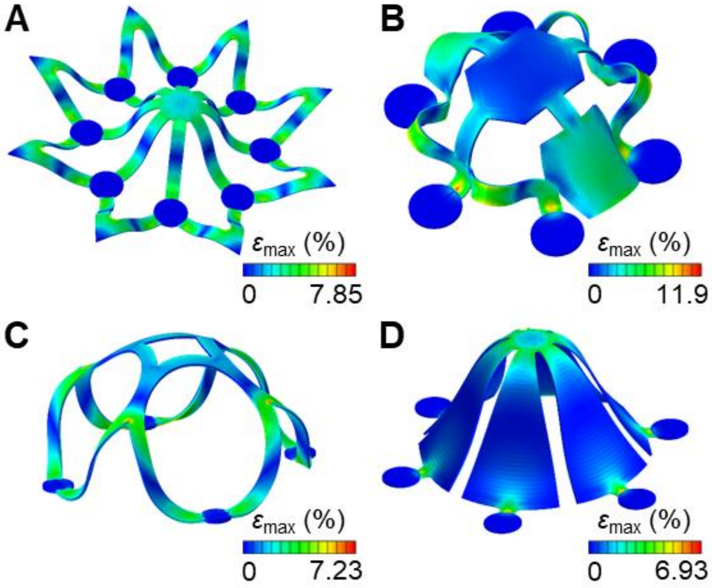

Fig. S11. Contour plots of the maximum principal strain for selected 3D microvascular structures presented in Fig. 2. (A–D) correspond to the third design in (A), the second in (B), the fourth in (A), and the third in (B) in Fig. 2, respectively.

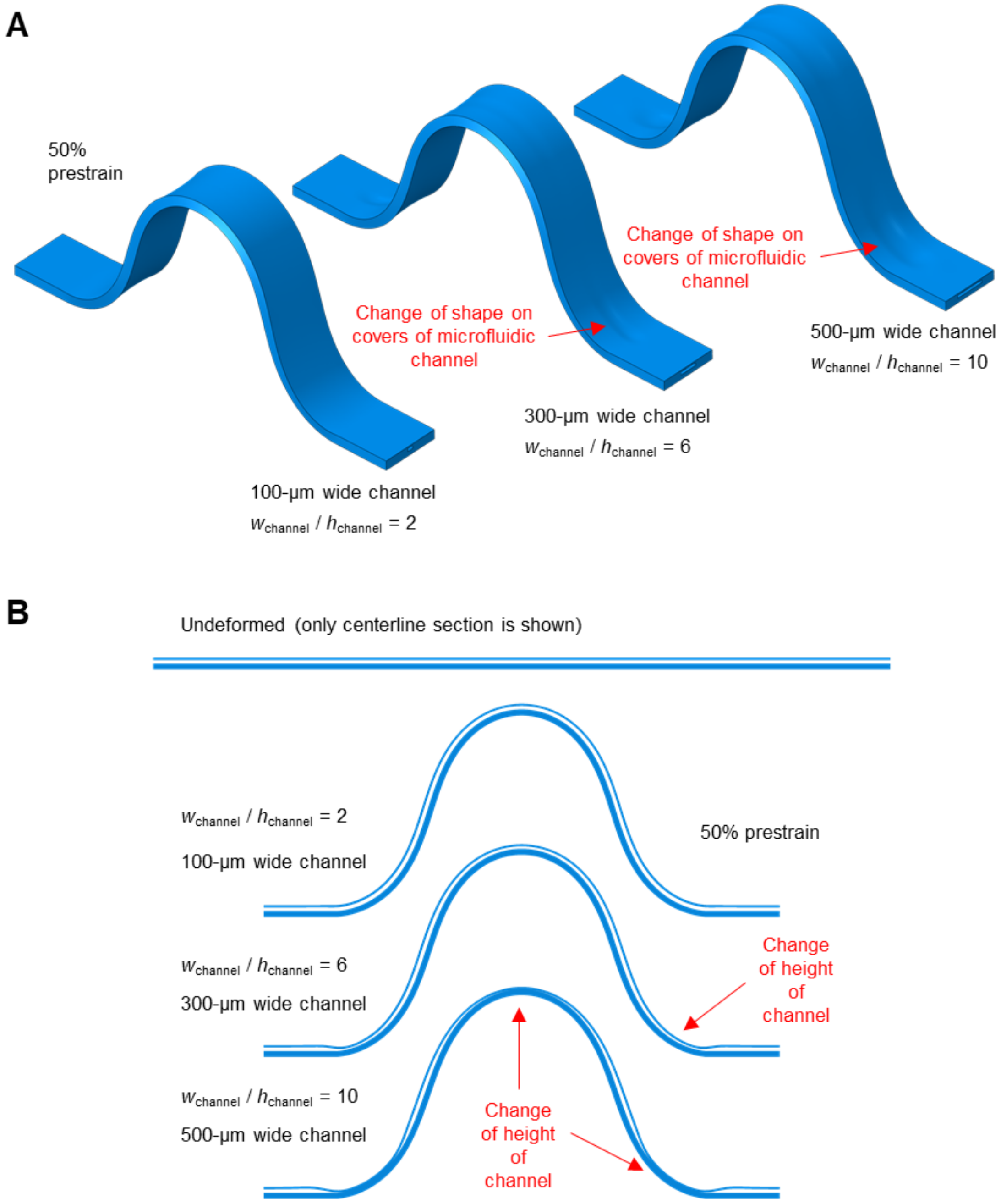

Fig. S12. 3D geometry of the microfluidic structure and associated deformation of microchannel, with different microchannel aspect ratios w_{channel} / h_{channel} (with fixed h_{channel} = 50 µm), during the 3D assembly process. FEA results from (A) 3D view and (B) centerline sectional view. This is a supplement to Fig. 2C, middle.

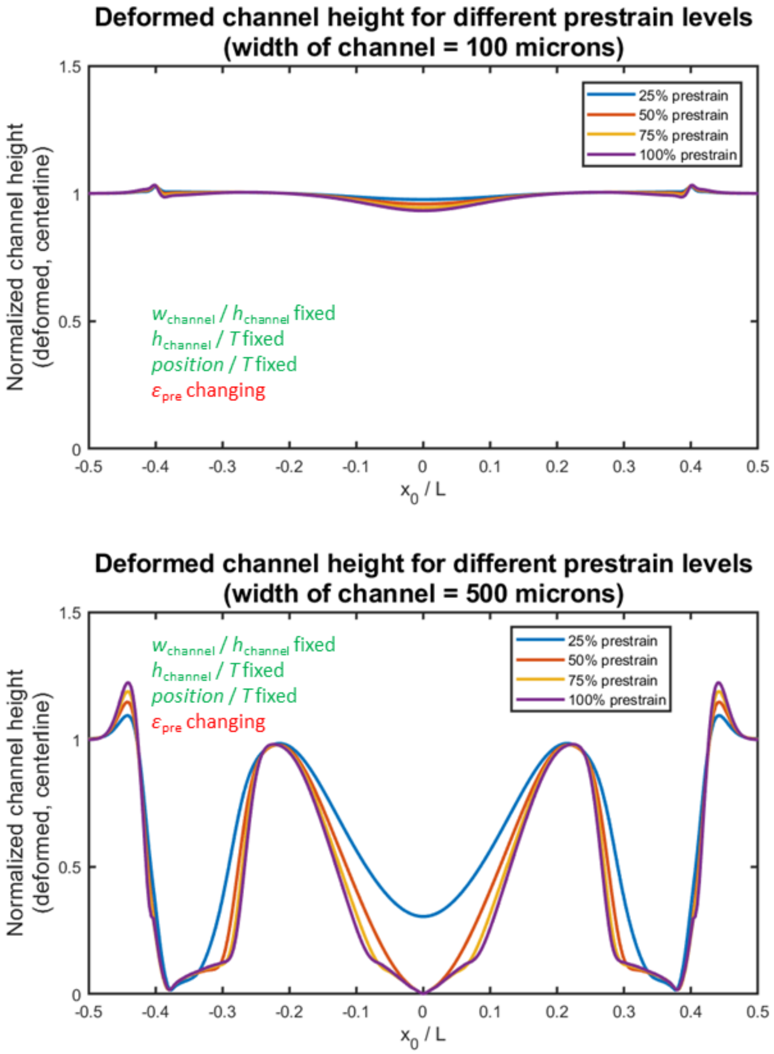

Fig. S13. Effect of prestrain on the deformation of microchannel, at two other different microchannel widths $w_{channel}$ (with fixed $h_{channel}$ = 50 µm), during 3D assembly process. This is a supplement to Fig. 2C, right.

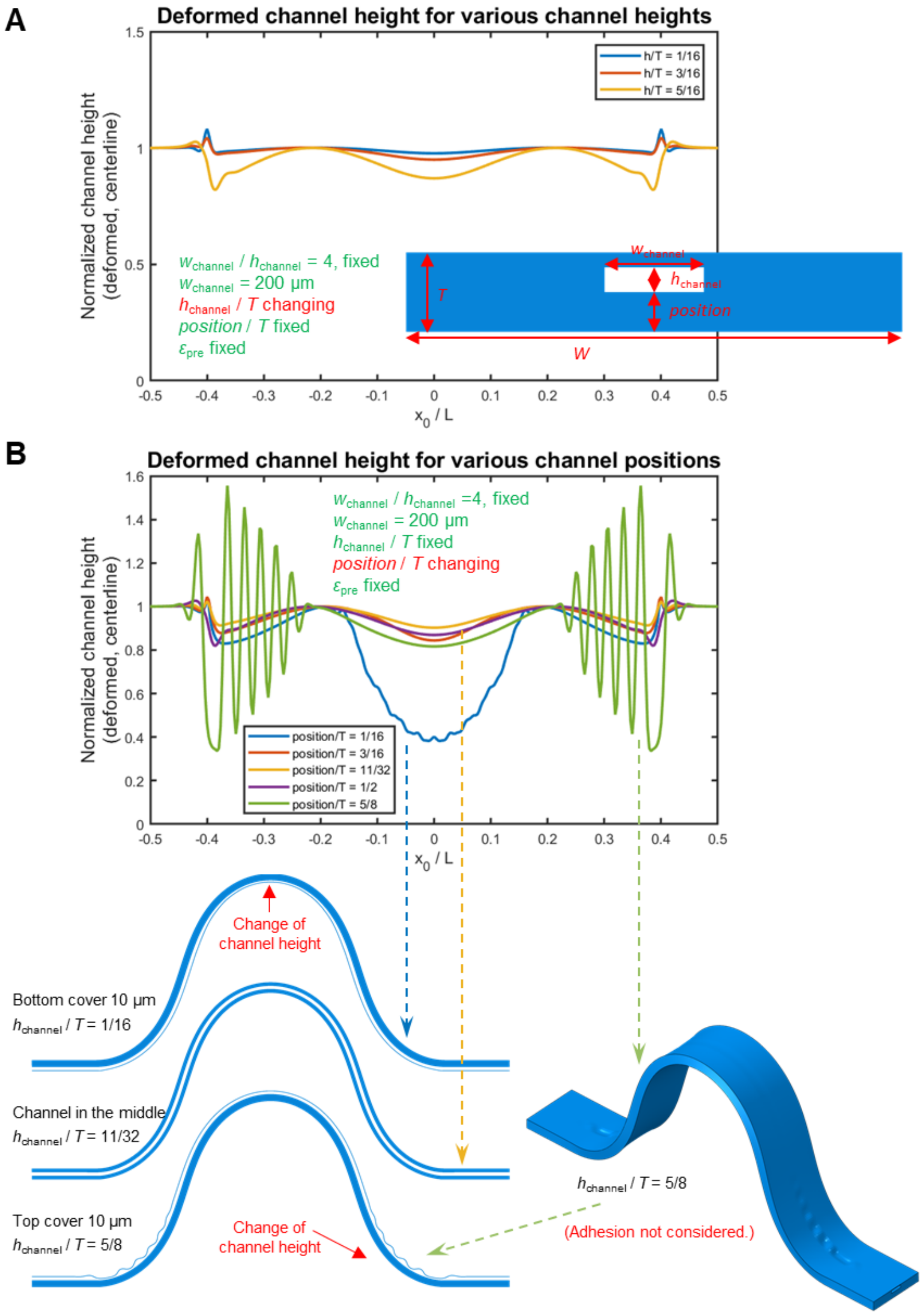

Fig. S14. Effects of channel height and channel position on the deformation of microchannels during 3D assembly. (A) Effect of channel height. (B) Effect of channel position. Adhesion between top and bottom channel walls is not considered in FEA.

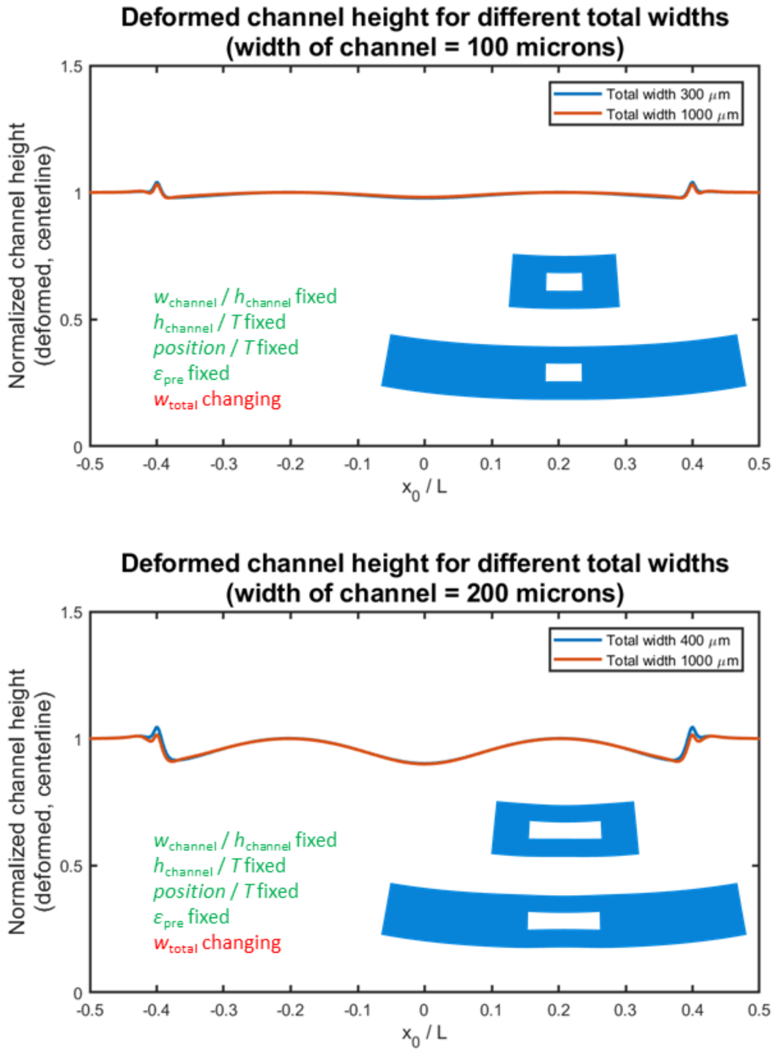

Deformed channel height for different total widths (width of channel = 100 microns)

Deformed channel height for different total widths (width of channel = 200 microns)

Fig. S15. Effect of total cross-sectional width on the deformation of microchannel, with two different microchannel widths $w_{channel}$ (with fixed $h_{channel}$ = 50 μm), during 3D assembly process. The deformed cross-sectional configurations at midspan ($x_0 = 0$) are shown as insets.

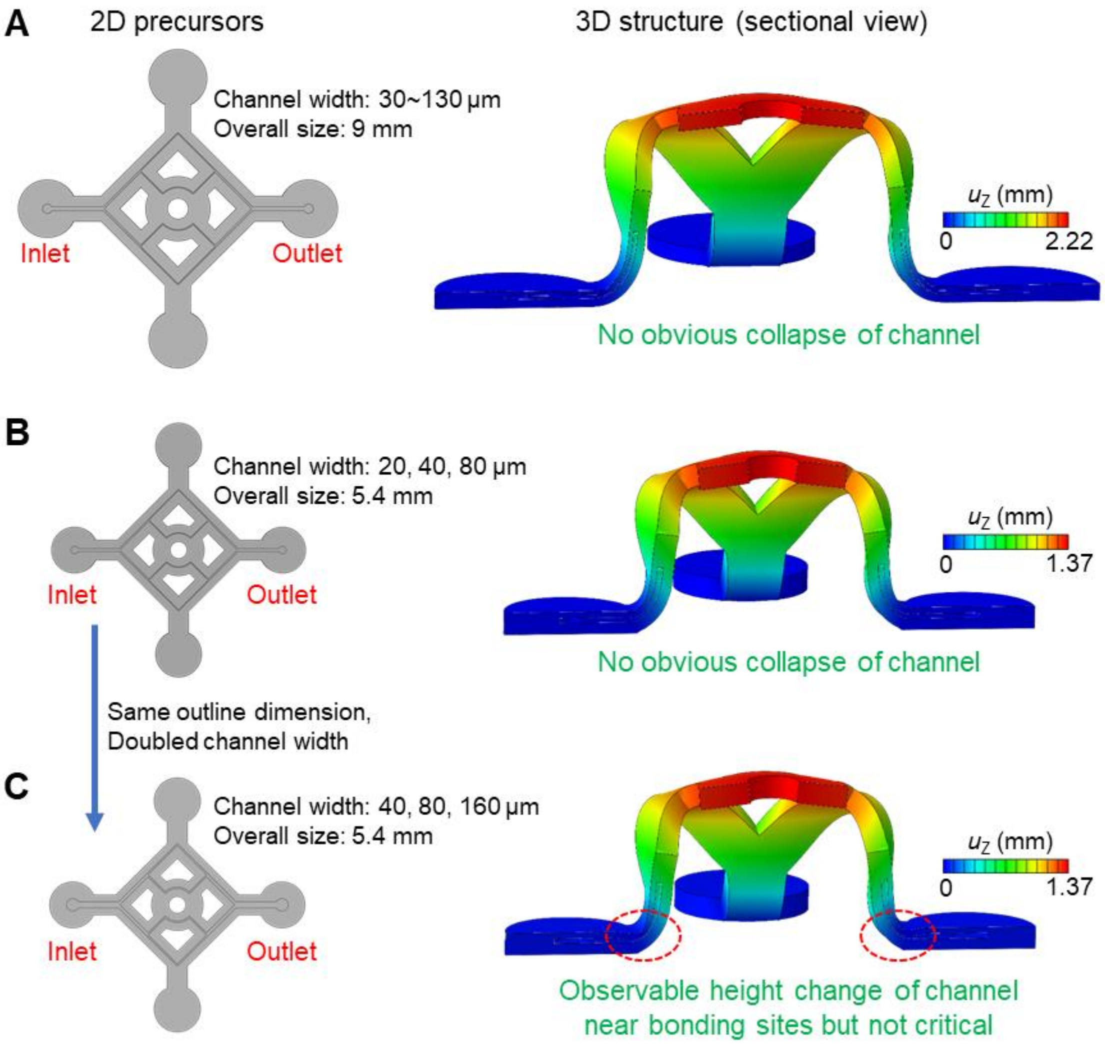

Fig. S16. Deformation of microchannels in the scalable table structures (medium 0.5x, and small 0.3x) in Fig. 3A. Microchannel height 50 µm. PDMS thickness 200 µm. Biaxial prestrain 50%.

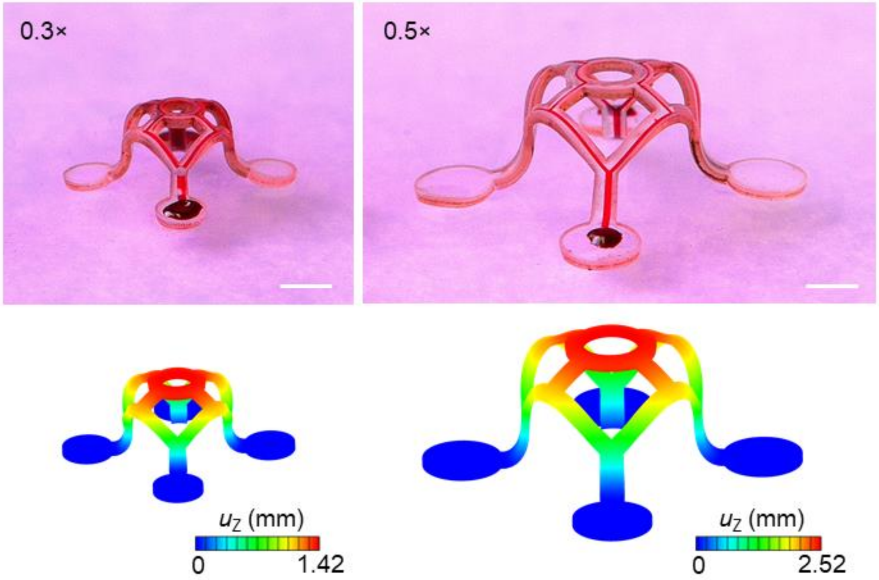

Fig. S17. Optical images and FEA contours of individual scalable table structures (small 0.3×, and medium 0.5×) in the multilayer assembly in Fig. 3B. Scale bars, 1 mm.

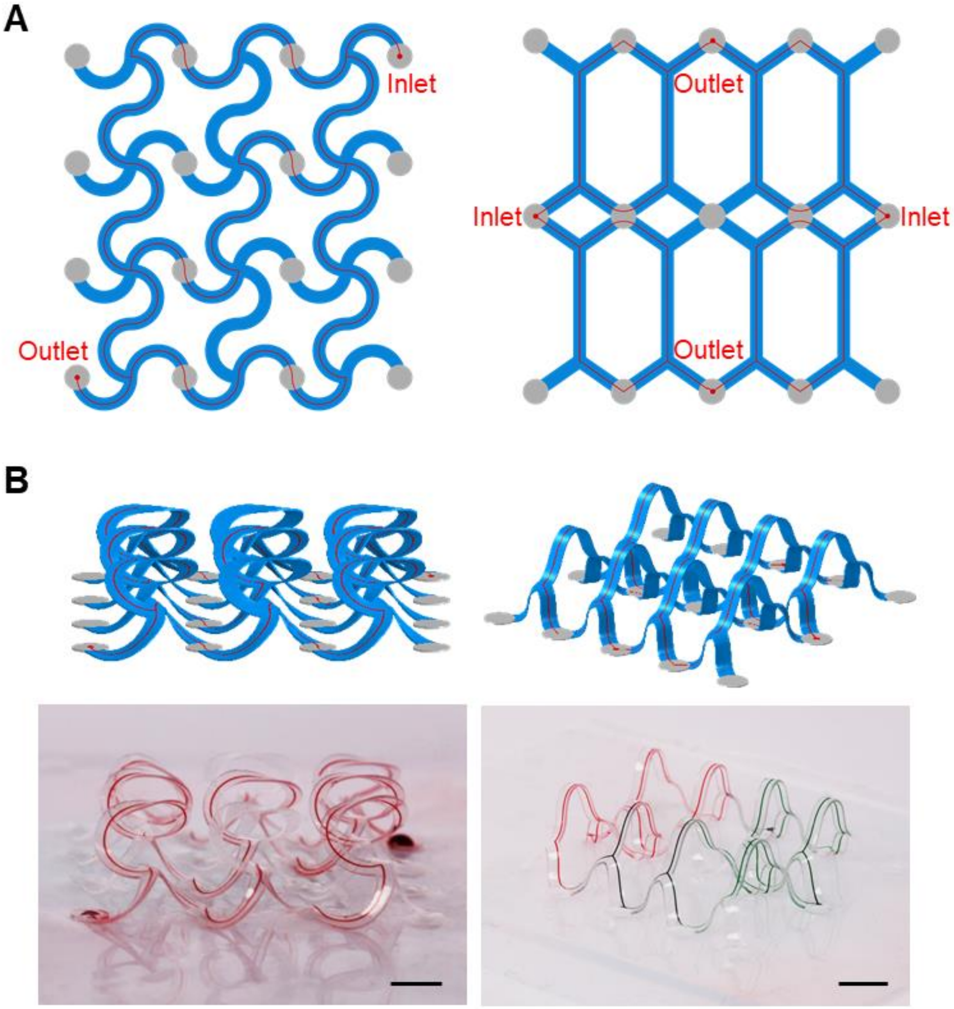

Fig. S18. Two examples of interconnected 3D microfluidic networks. (A) 2D precursors of interconnected microfluidic networks and (B) 3D interconnected microfluidic networks observed from a different 3D view. Scale bars, 5 mm.

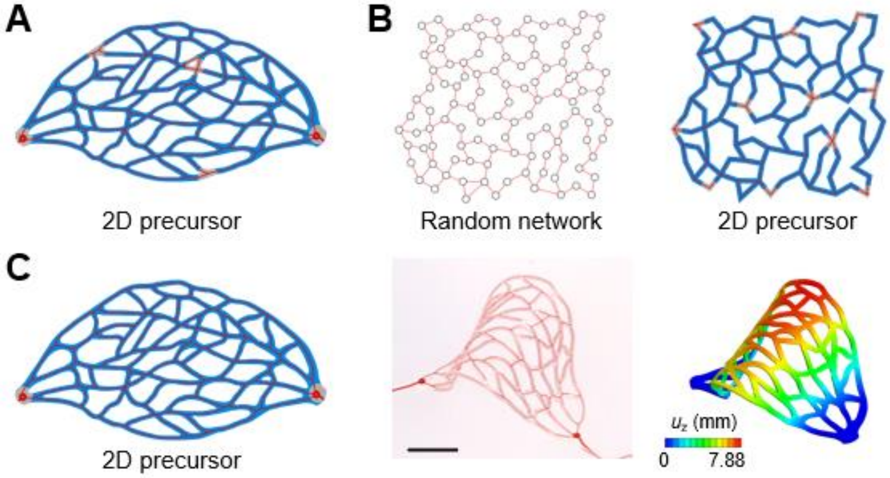

Fig. S19. Assembly of 3D irregular networks by compressive buckling. (A) 2D microfluidic precursor (with five randomly assigned bonding sites, each enclosed by a circle of constant radius) of the irregular 3D network in Fig. 3D, left. (B) 2D microfluidic precursor of the random 3D network in Fig. 3D, right. (C) 3D irregular geometry assembled from a same 2D simplified capillary network with (A), with only two bonding sites at the ends. Scale bar, 5 mm.

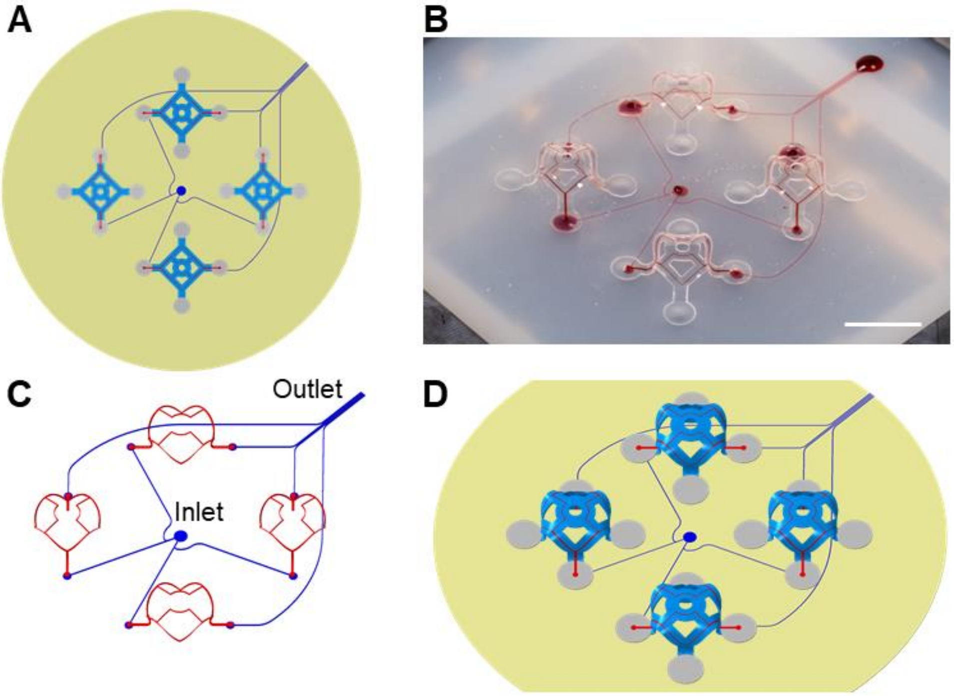

Fig. S20. Integrated array of identical 3D microvascular structures on an elastomer substrate with embedded microfluidic channels. (A) 2D microfluidic precursors aligned to a 50% biaxially prestretched elastomer substrate. (B) An optical image of the 3D microvascular system. (C, D) FEA results showing the predicted geometries of 3D microchannel network (C) and 3D microfluidic architectures (D), respectively. Scale bar, 10 mm.

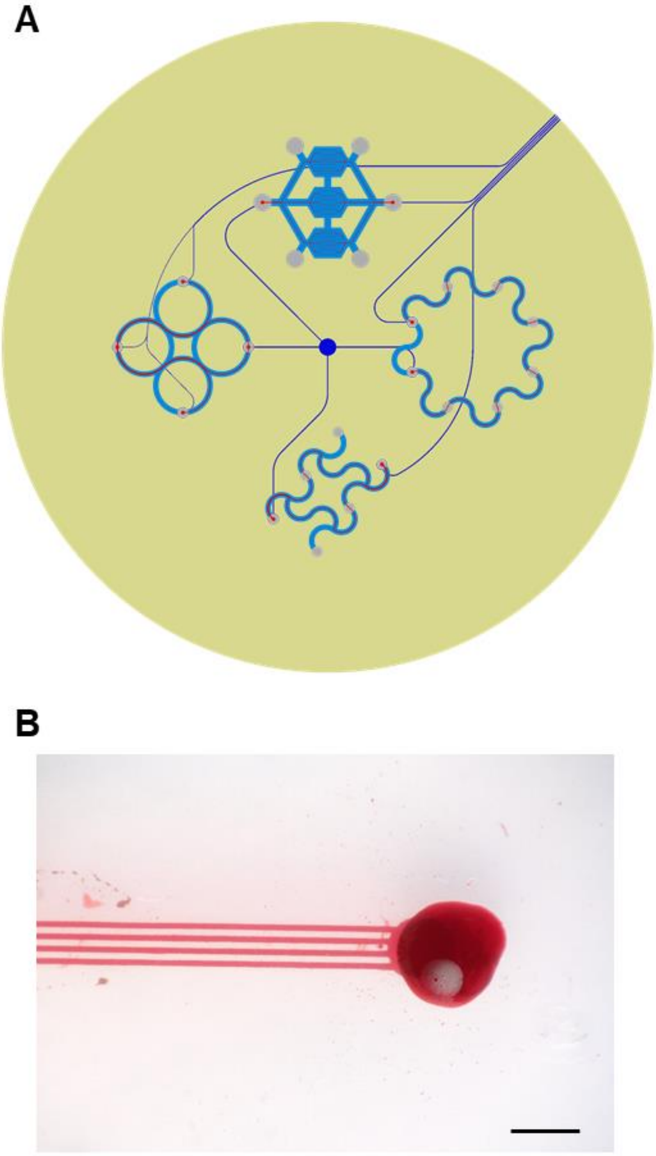

Fig. S21. An integrated 3D microfluidic network consisting of 3D microfluidic architectures and elastomer substrate with embedded microchannels. (A) 2D microfluidic precursors aligned to a 50% biaxially prestretched elastomer substrate with embedded microfluidic channels. (B) A magnified optical image of the outlet of microfluidic channels. Scale bar, 1 mm.

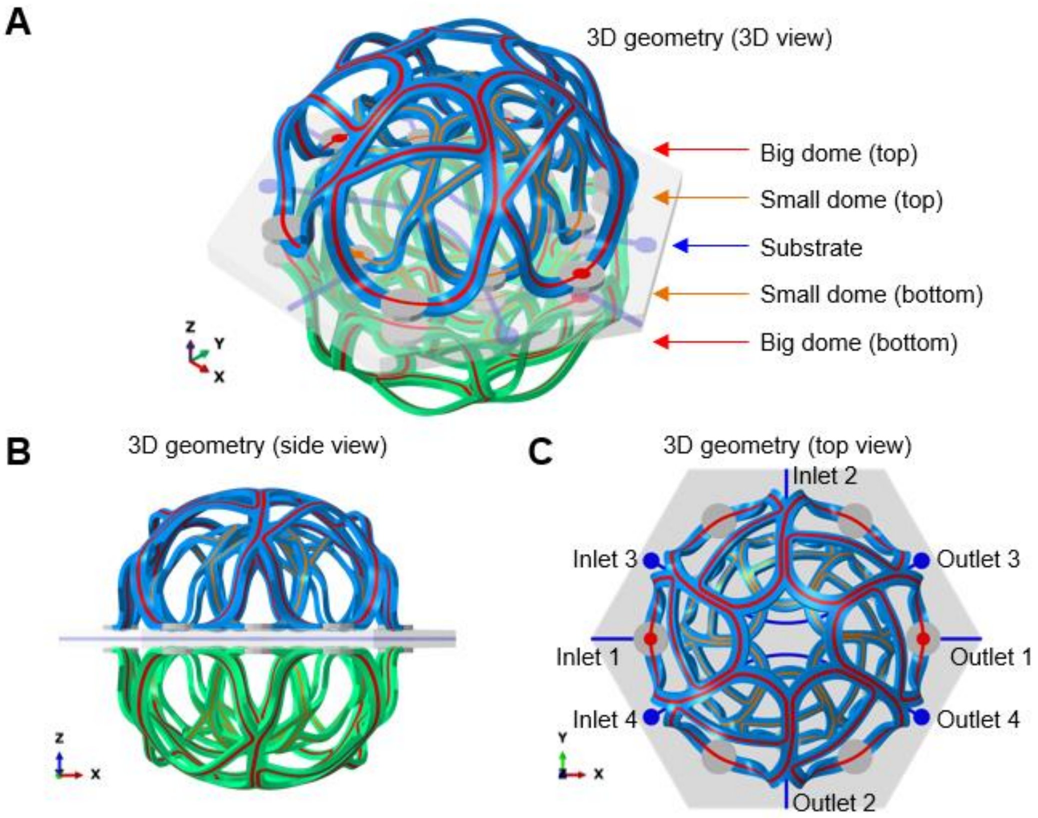

Fig. S22. Five-layer stack of 3D microfluidic structures demonstrating complex topology. The substrate also has embedded microfluidic channels. 3D view (A), side view (B) and top view (C) illustrations of the design of multilayer microfluidic structures.

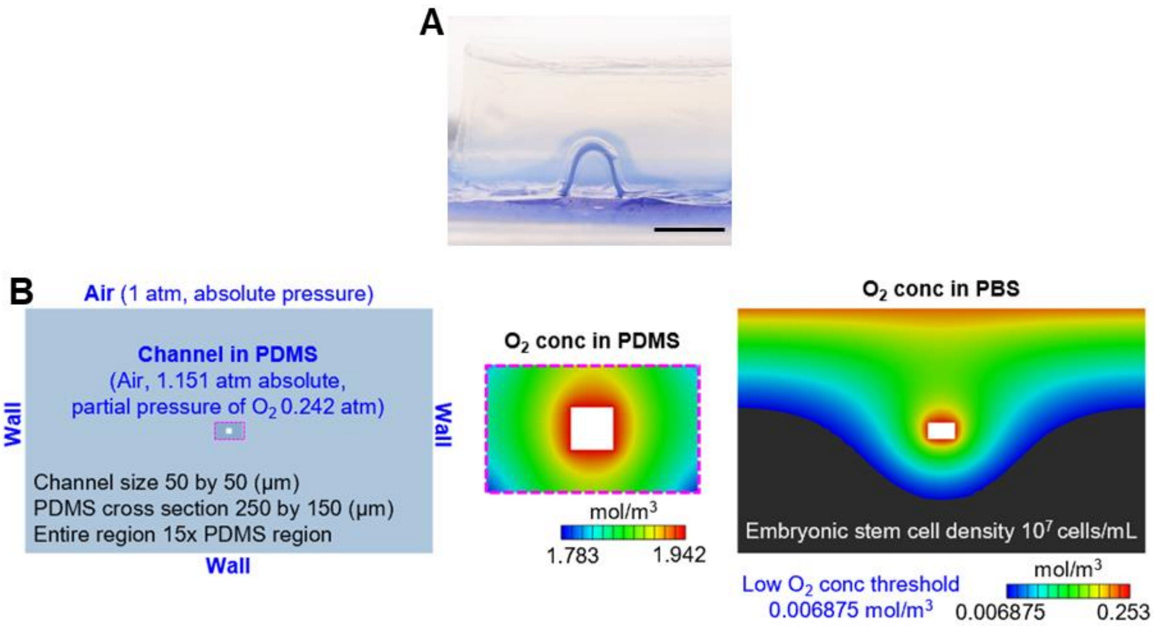

Fig. S23. 3D microfluidic structures as artificial vascular networks for transporting oxygen and maintaining oxygen concentration for cell culture. (A) Image of oxygen delivery to a block of oxygen-sensitive hydrogel with oxygen-rich perfluorocarbon flowing inside a 3D microfluidic channel. (B) Results of an FEA diffusion model for the oxygen concentration in a 3D structure (PDMS) and its surrounding PBS (at room temperature) considering oxygen consumption of cells. (B, left) Schematic illustration of the FEA diffusion model. (B, middle) The oxygen concentration in the 3D microfluidic structure (cross-section). (B, right) The oxygen concentration in the PBS.

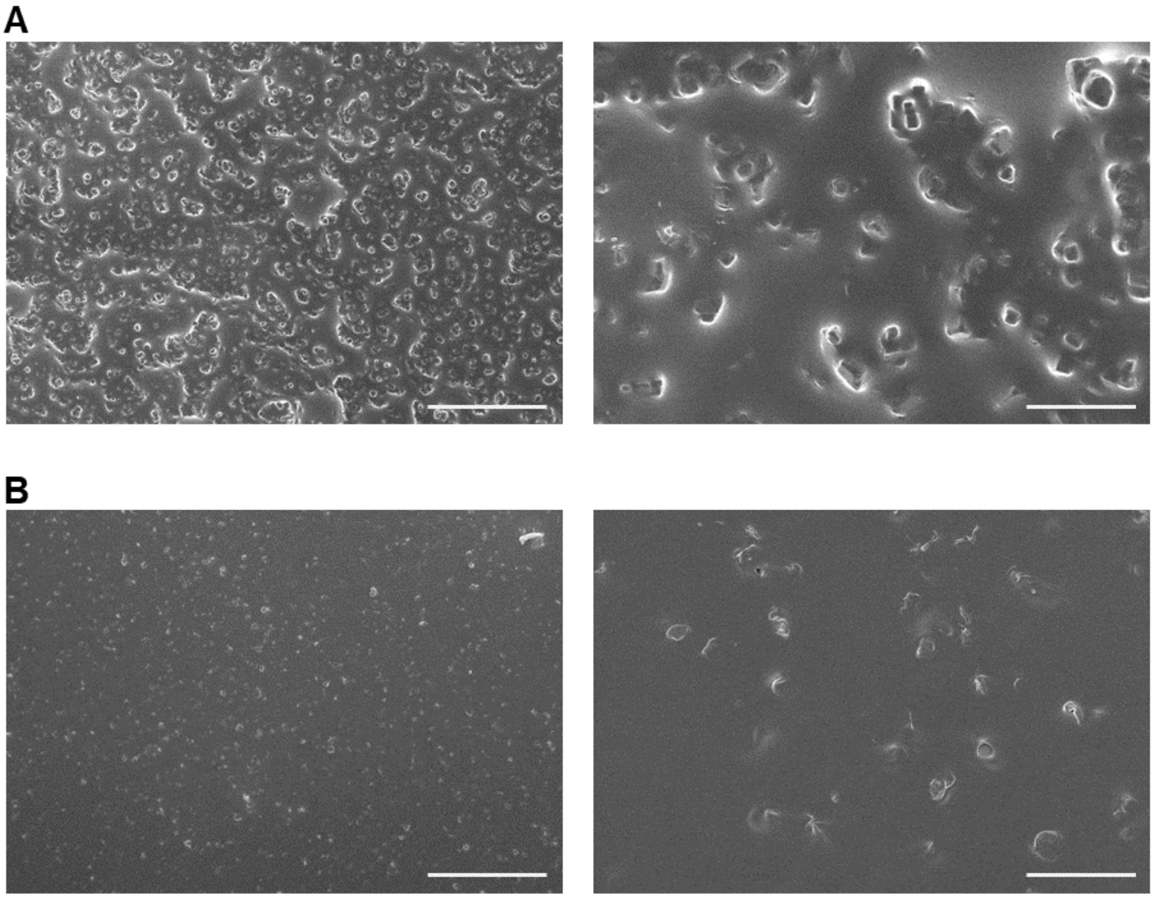

Fig. S24. Additional SEM images of the top and bottom surfaces of microporous PDMS film (before dissolving NaCl). (A) Top surface. (B) Bottom surface. Scale bars, 150 μm in (A, left) and (B, left), and 25 μm in (A, right) and (B, right).

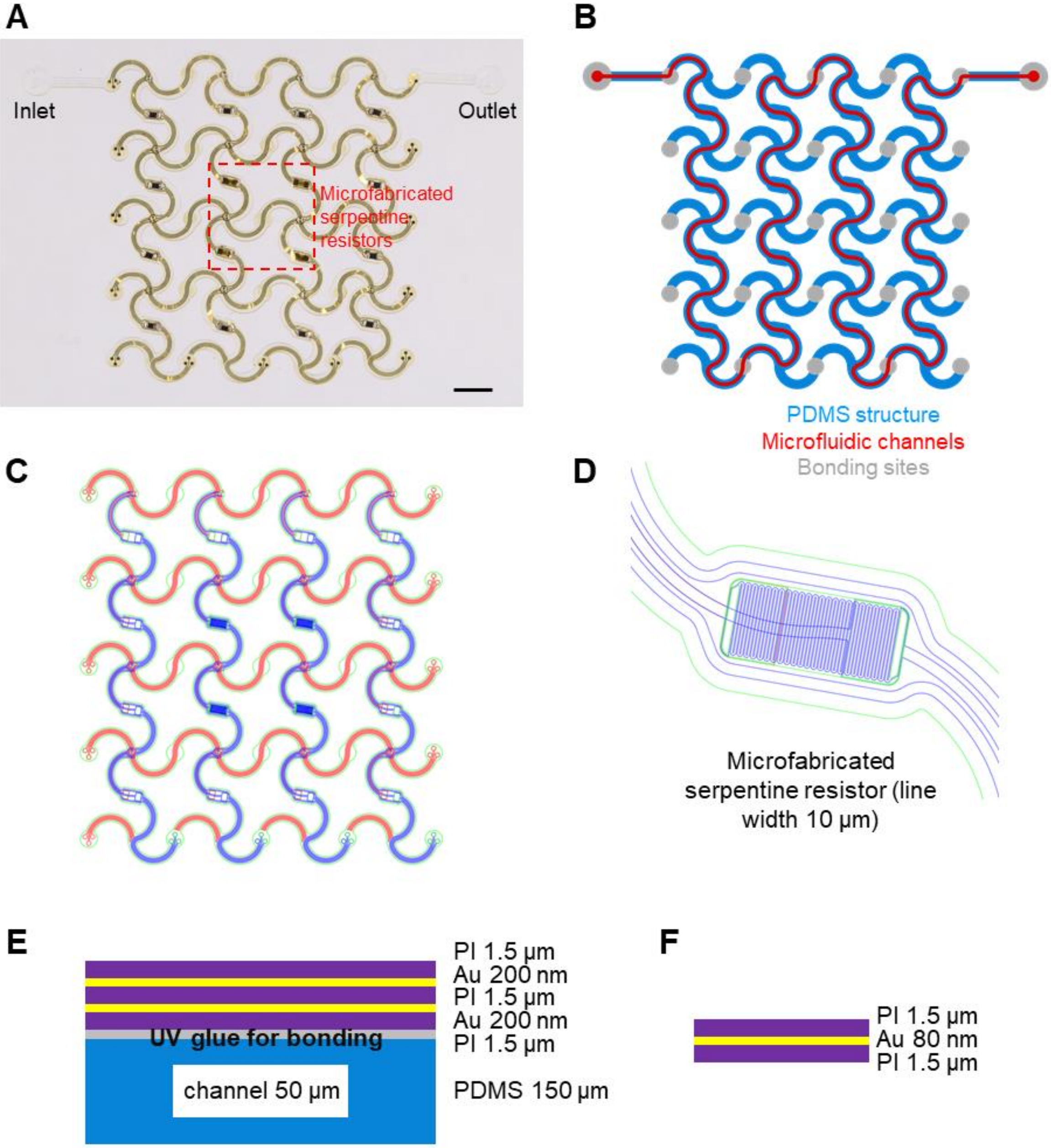

Fig. S25. 2D precursors of microfluidic and electronic parts and cross-sectional details of the microfluidics-electronics hybrid platform. (A) Optical image of the aligned electronic precursor on top of a microfluidic precursor. (B) Schematic illustration of the 2D microfluidic precursor. (C) Schematic illustration of the 2D precursor of gold traces encapsulated in PI layers. (D) Magnified schematic illustration of a serpentine heater/thermistor. (E) Thickness profile of the microfluidics-electronics hybrid platform. (F) Thickness profile of a serpentine resistor. Scale bar, 2 mm.

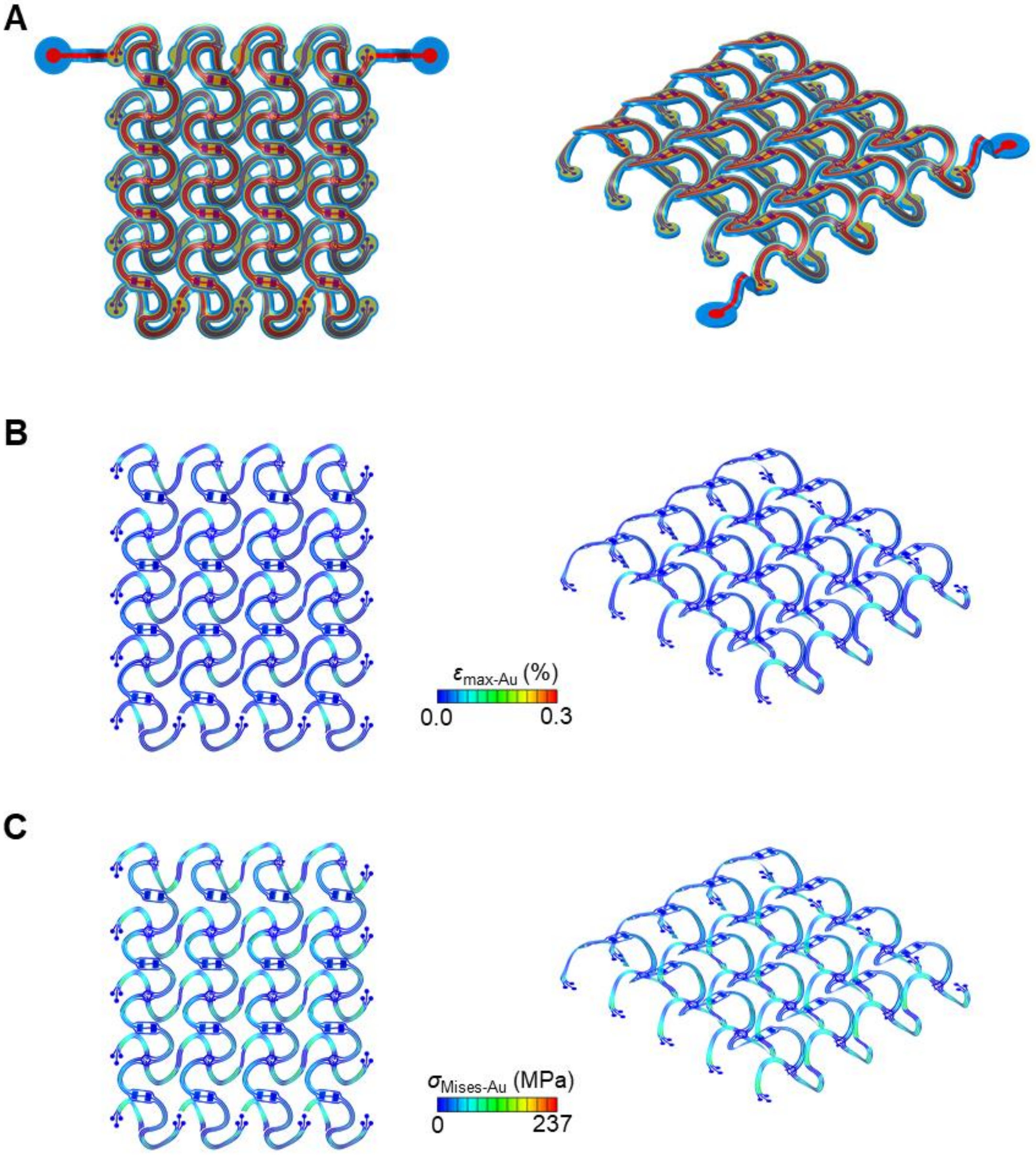

Fig. S26. 3D geometry of and strain/stress distributions in the PI/Au/PI/Au/PI circuit layer within the 3D hybrid microfluidic-electronic platform. (A) Schematic illustration showing the deformed shape of the 3D hybrid microfluidic-electronic platform from a top view (left) and a 3D view (right). Contours of maximum principal strain of gold (B) and von Mises stress of gold (C) in the PI/Au/PI/Au/PI circuit layer. The electronic layer and the microfluidic layer are bonded at selective locations (e.g., bonding sites, conjunctions of rows and columns, and the midspans on the second floor of the double-floor helical structure) in consistence with experiment. The results in (B) and (C) indicate the gold layers are within elastic regime (with yield strain of 0.3% and yield stress of 237 MPa for gold) after 3D assembly.

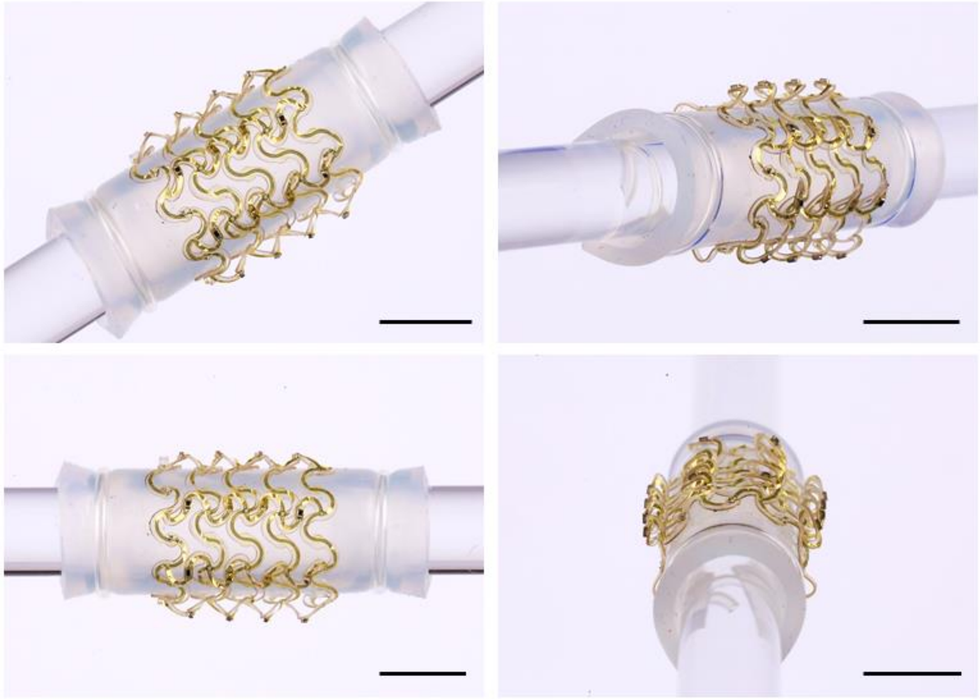

Fig. S27. Soft, stretchable hybrid system wrapped around a glass rod (6 mm in diameter) together with the elastomer substrate. Scale bars, 6 mm.

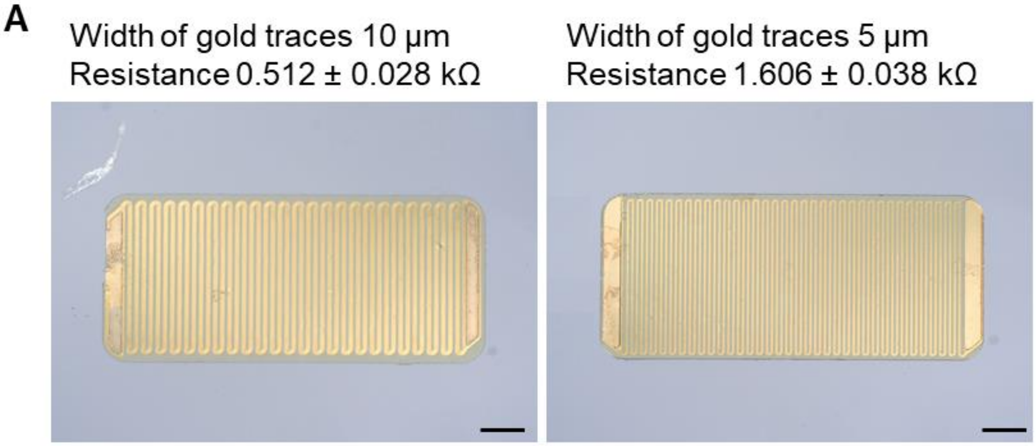

Width of gold traces 10 μm
Resistance 0.512 ± 0.028 kΩ

Width of gold traces 5 μm
Resistance 1.606 ± 0.038 kΩ

B

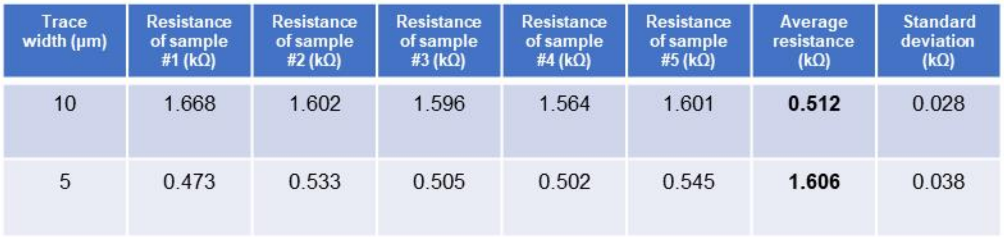

Trace width (μm)	Resistance of sample #1 (kΩ)	Resistance of sample #2 (kΩ)	Resistance of sample #3 (kΩ)	Resistance of sample #4 (kΩ)	Resistance of sample #5 (kΩ)	Average resistance (kΩ)	Standard deviation (kΩ)
10	1.668	1.602	1.596	1.564	1.601	**0.512**	0.028
5	0.473	0.533	0.505	0.502	0.545	**1.606**	0.038

Fig. S28. Two versions of attachable serpentine Au traces as heaters and temperature sensors. (A) Optical images of serpentine Au traces with two different widths. (B) Measurement of resistance of serpentine Au traces. Scale bars, 100 μm.

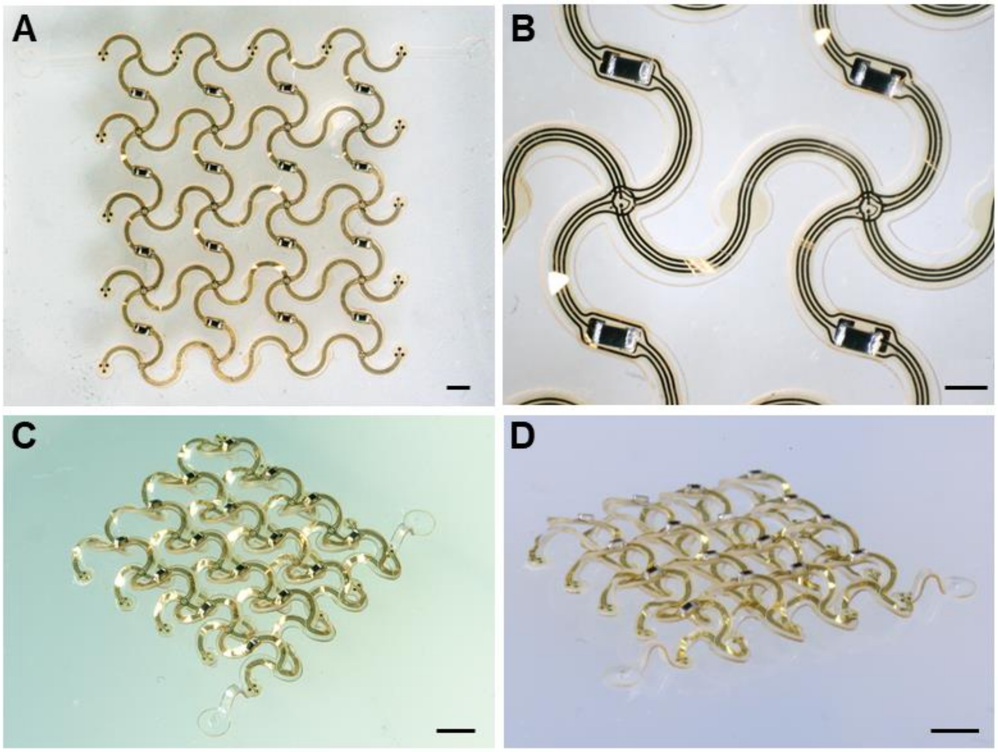

Fig. S29. 3D microfluidics-electronics hybrid platform with 4-by-4 SMD 0201 resistors. Scale bars, 1 mm in (A), 500 μm in (B), and 2 mm in (C, D).

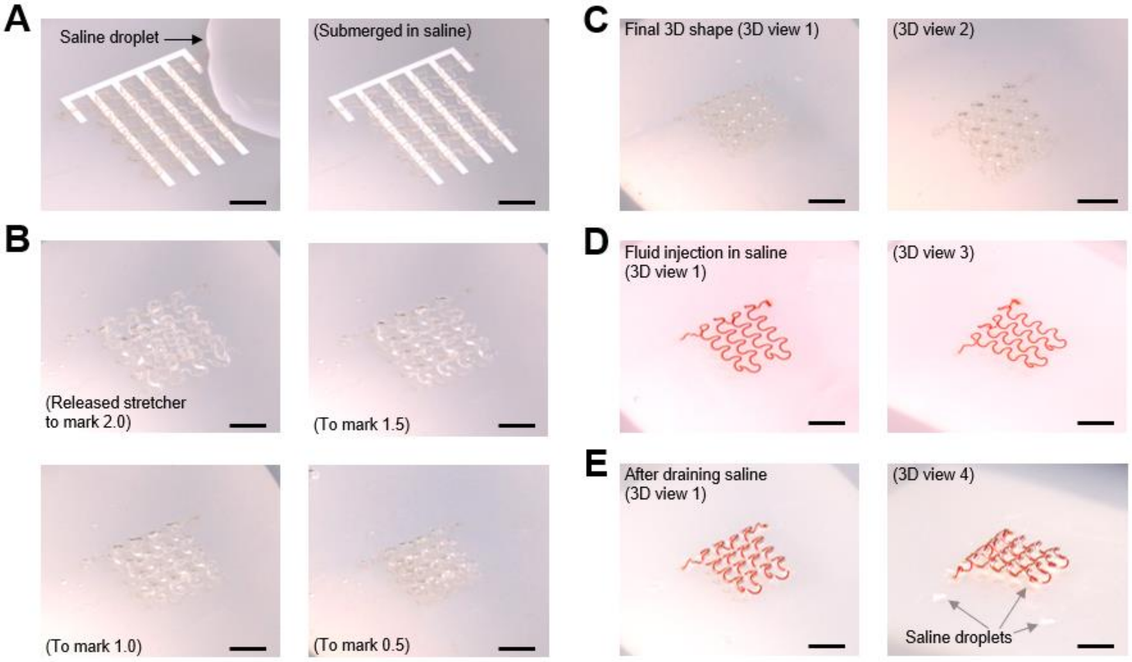

Fig. S30. Assembly of a 3D microfluidic array in saline solution (NaCl in water, 0.9% w/w). (A) 2D microfluidic precursor before and after submerging in saline solution. A piece of laser cut paper can be used to prevent the nonbonding regions from adhering to the substrate. (B) Intermediate states during the 2D-to-3D shape transformation, all in saline solution. (C) Final 3D shape in saline solution. (D) Injection of water dyed in red directly in saline solution using a syringe needle. (E) 3D geometry, with the microchannel filled with water dyed in red, after partially draining the saline solution. Scale bars, 5 mm.

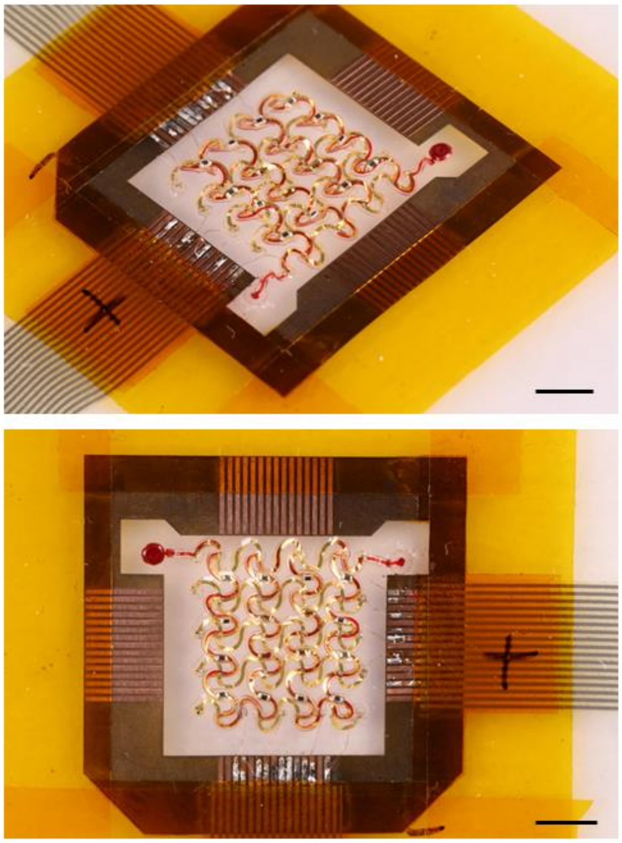

Fig. S31. Injection of water dyed in red into the 3D microchannel in the hybrid system. A customized flexible PCB connects the 3D hybrid system with power supply and associate electric circuit. Scale bars, 4 mm.

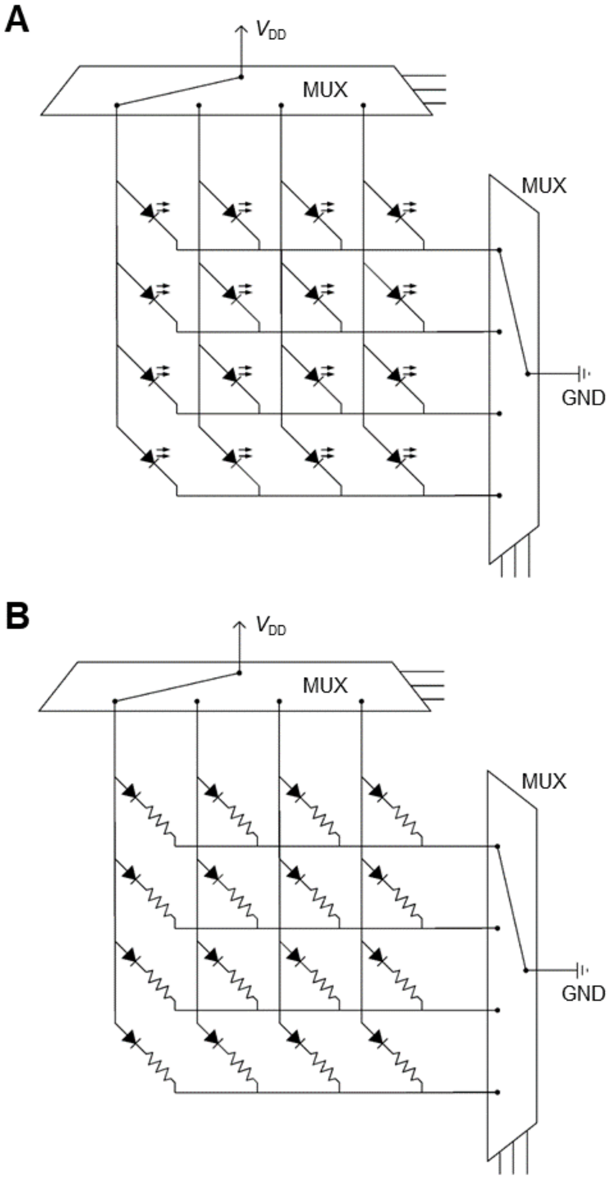

Fig. S32. Multiplexing circuit for the 4×4 arrays of μ-ILEDs and resistive heaters, with capability of individually addressing. (A) Multiplexing circuit for the array of μ-ILEDs. (B) Multiplexing circuit for the array of resistive heaters.

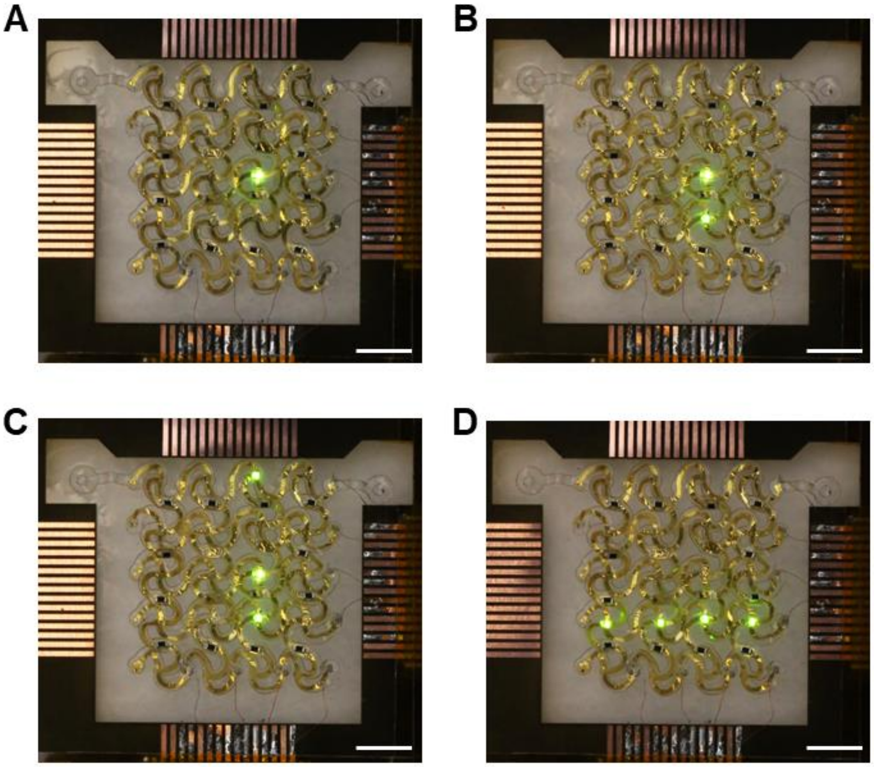

Fig. S33. Lighting of μ-ILEDs in the hybrid system. The number of lighted μ-ILEDs is 1, 2, 3, and 4 in A–D, respectively. A customized flexible PCB connects the 3D hybrid system with power supply. Scale bars, 3 mm.

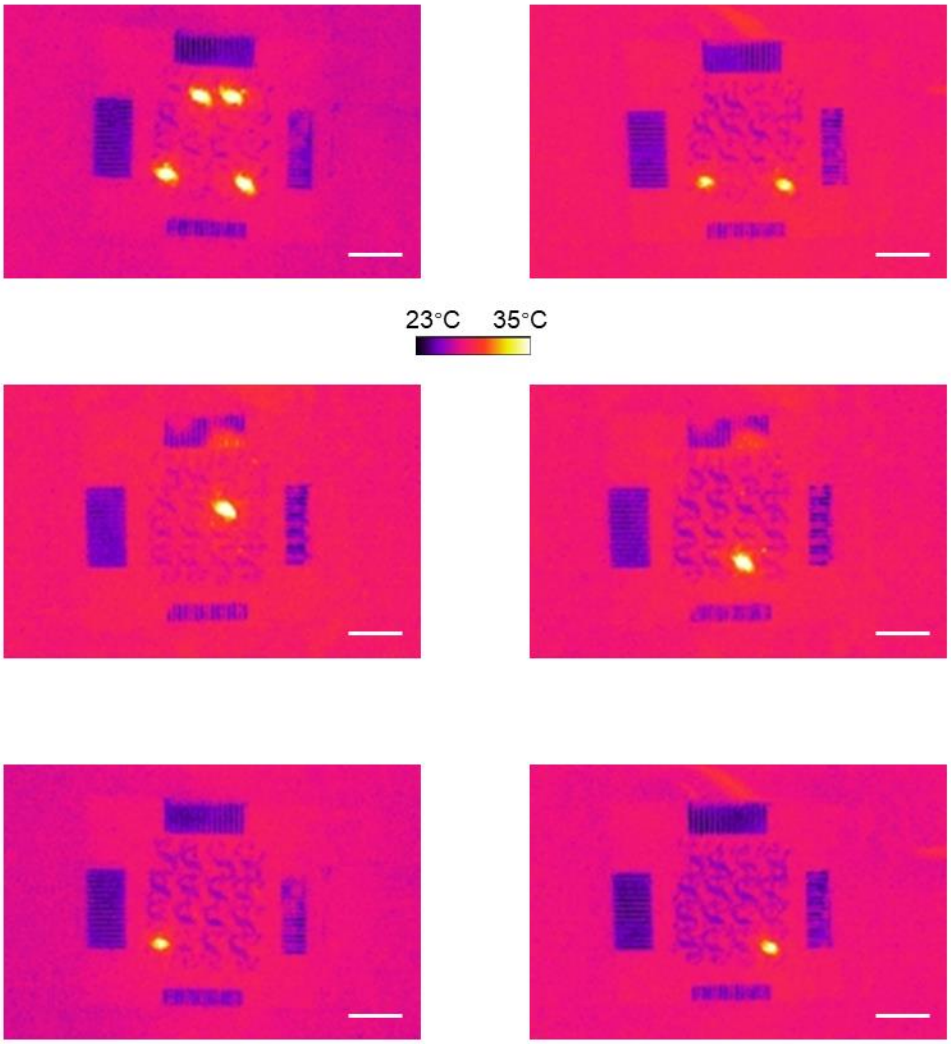

Fig. S34. Infrared images showing the localized heating by integrated heaters in the hybrid system. Scale bars, 5 mm.

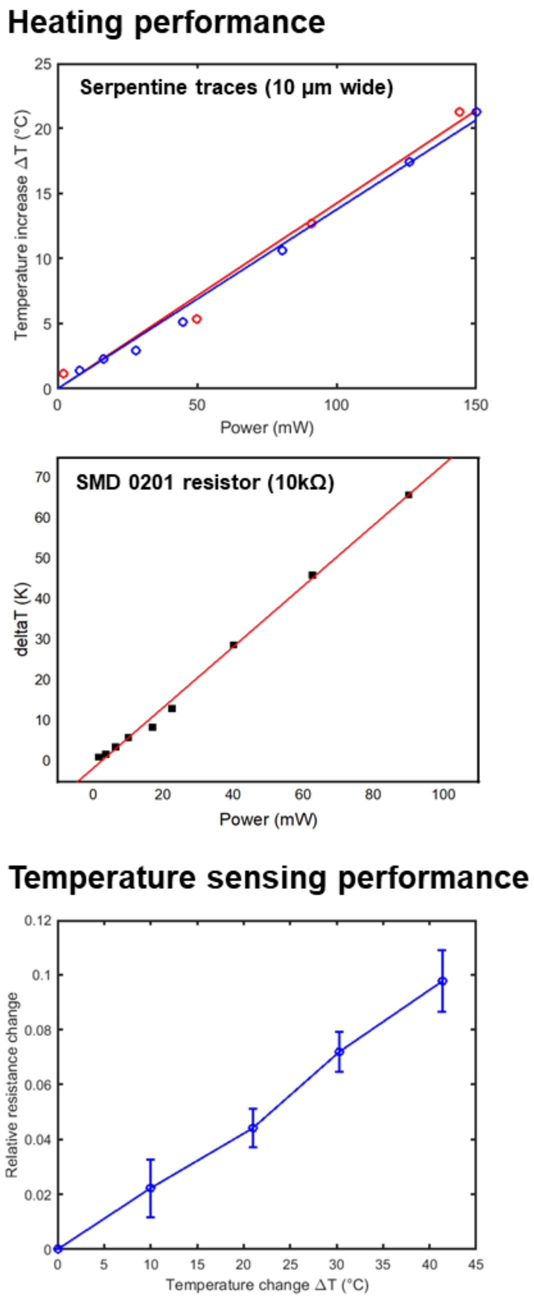

Fig. S35. Heating and temperature sensing performances.

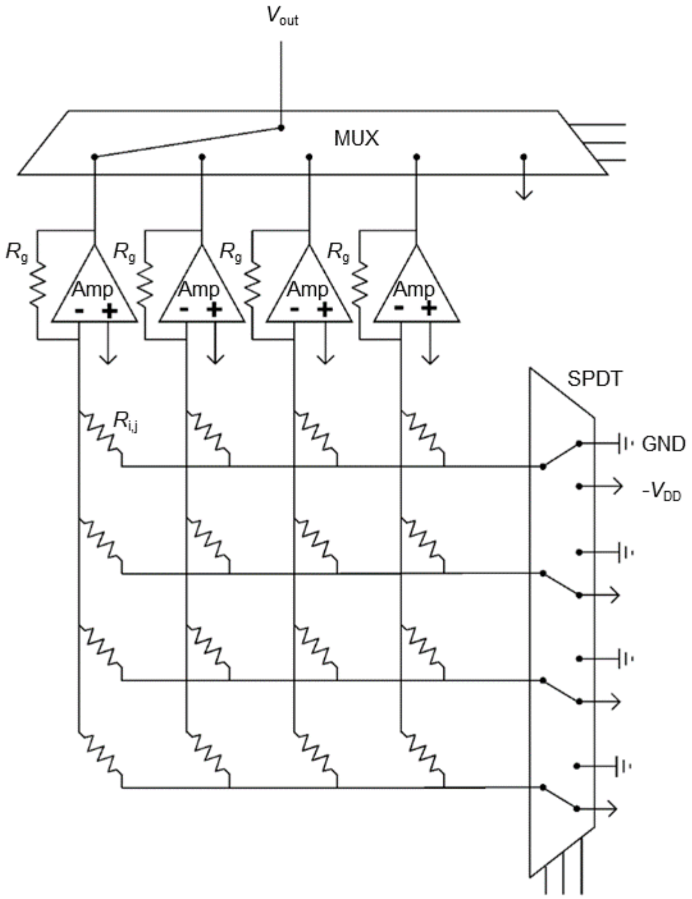

Fig. S36. Multiplexing circuit for the 4×4 array of temperature sensors (thermistors).

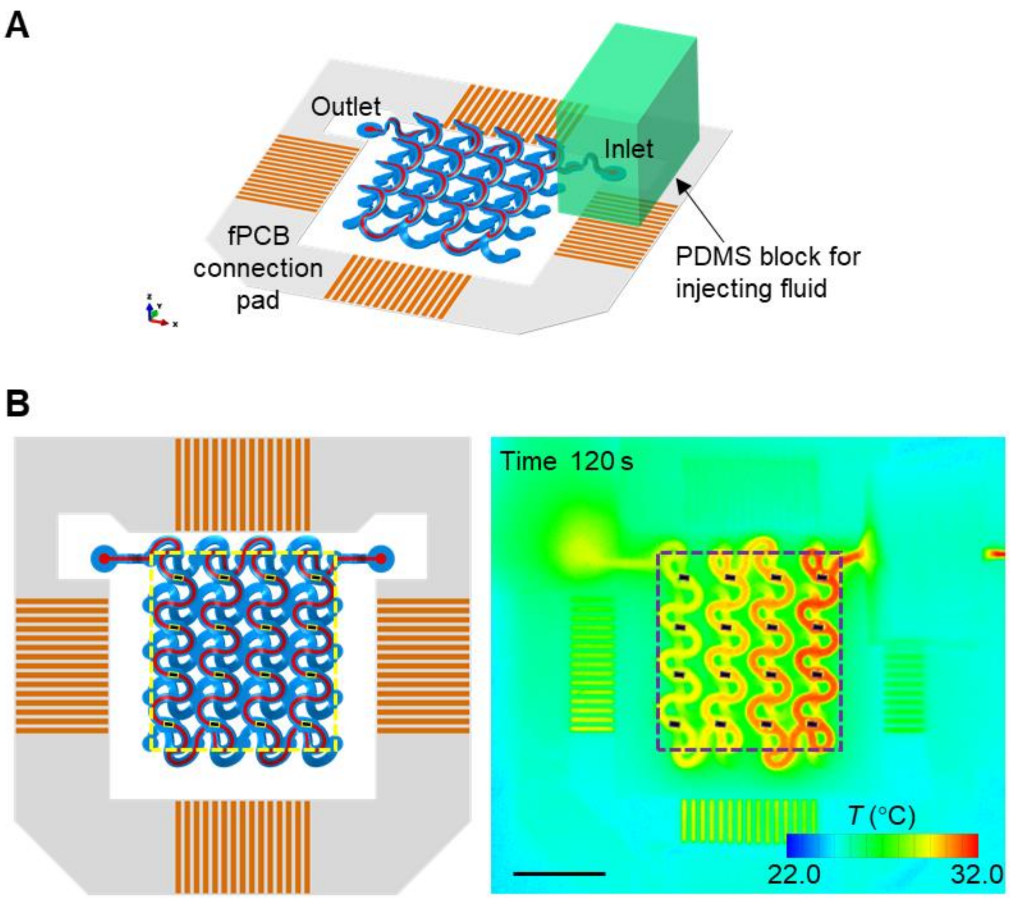

Fig. S37. Schematic of 3D hybrid system for temperature mapping during injection of hot water. (A) Schematic of device setup. (B) Top view comparison of the predicted 3D shape of microchannel and locations of thermistors by FEA with those from an IR image. Scale bar, 5 mm.

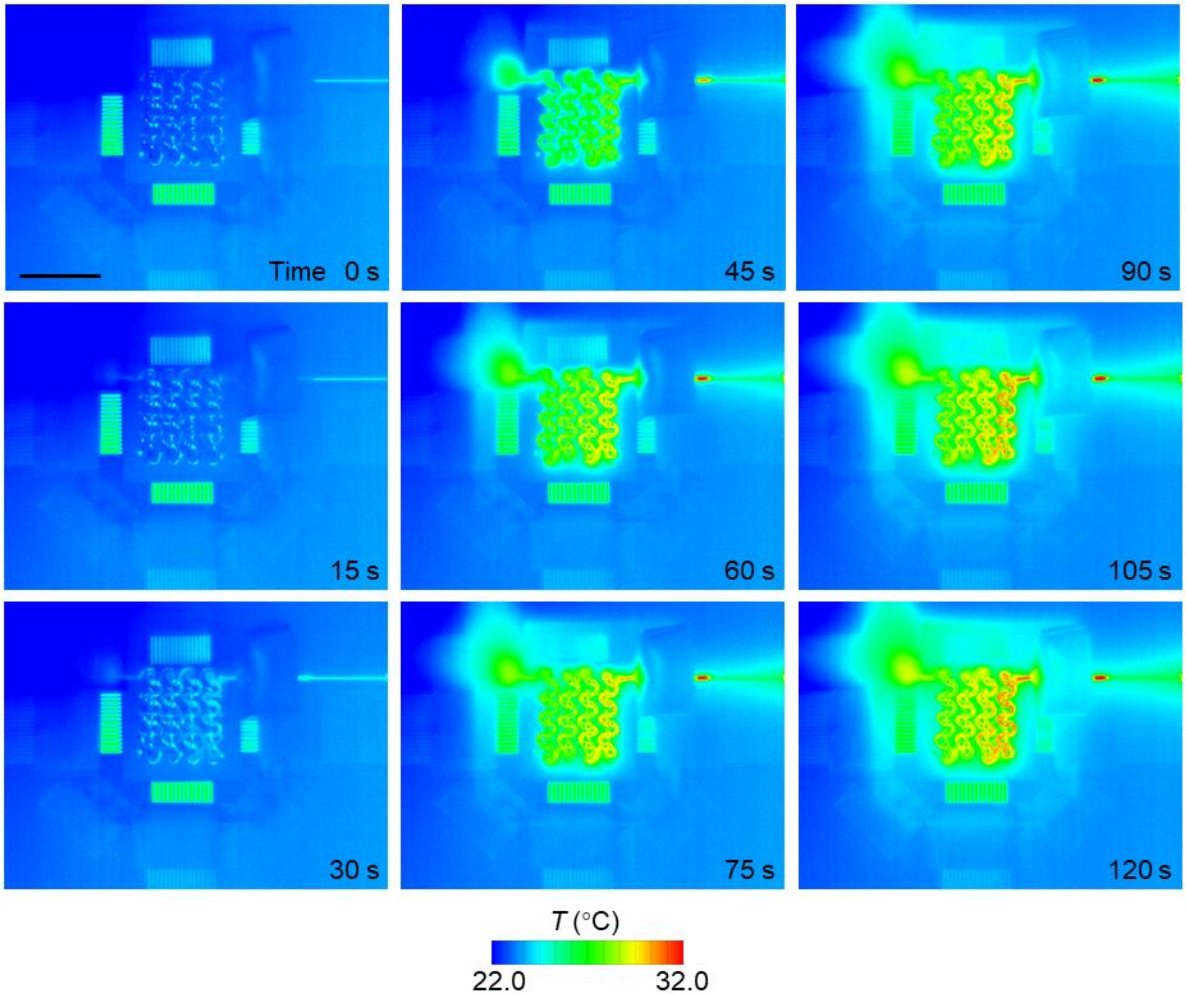

Fig. S38. Sequential infrared thermal images of a 3D hybrid system during injection of hot water. The initial base temperature is ~23.6 °C. The PI-Au circuit may block the visualization of temperature change on the PDMS structure. Scale bar, 10 mm.

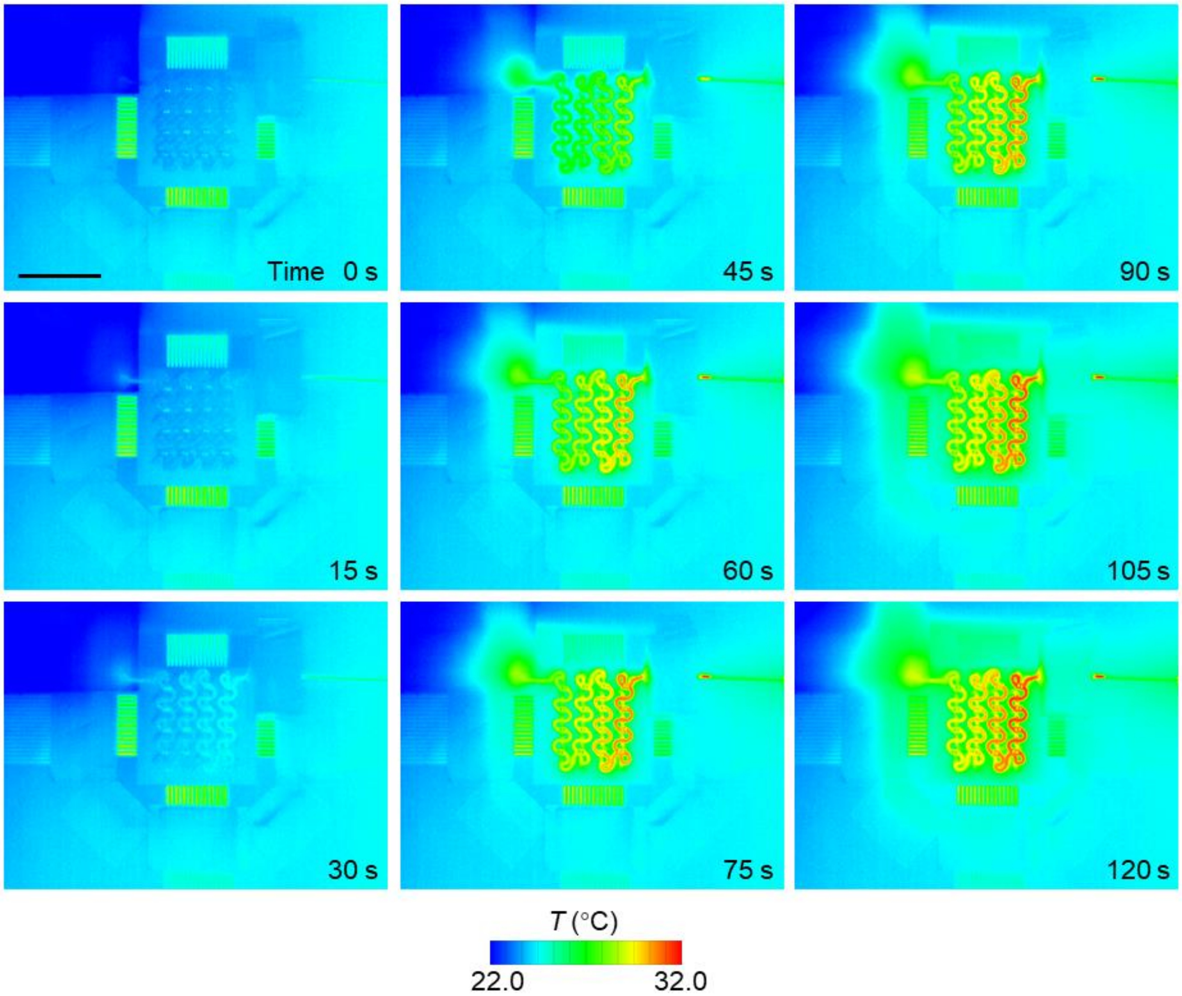

Fig. S39. Sequential infrared thermal images of a similar 3D system during injection of hot water. The initial base temperature is ~24.4 °C. The PI-Au circuit is removed to facilitate the visualization of temperature change on the PDMS structure. Scale bar, 10 mm. This shows the same result as movie S5.

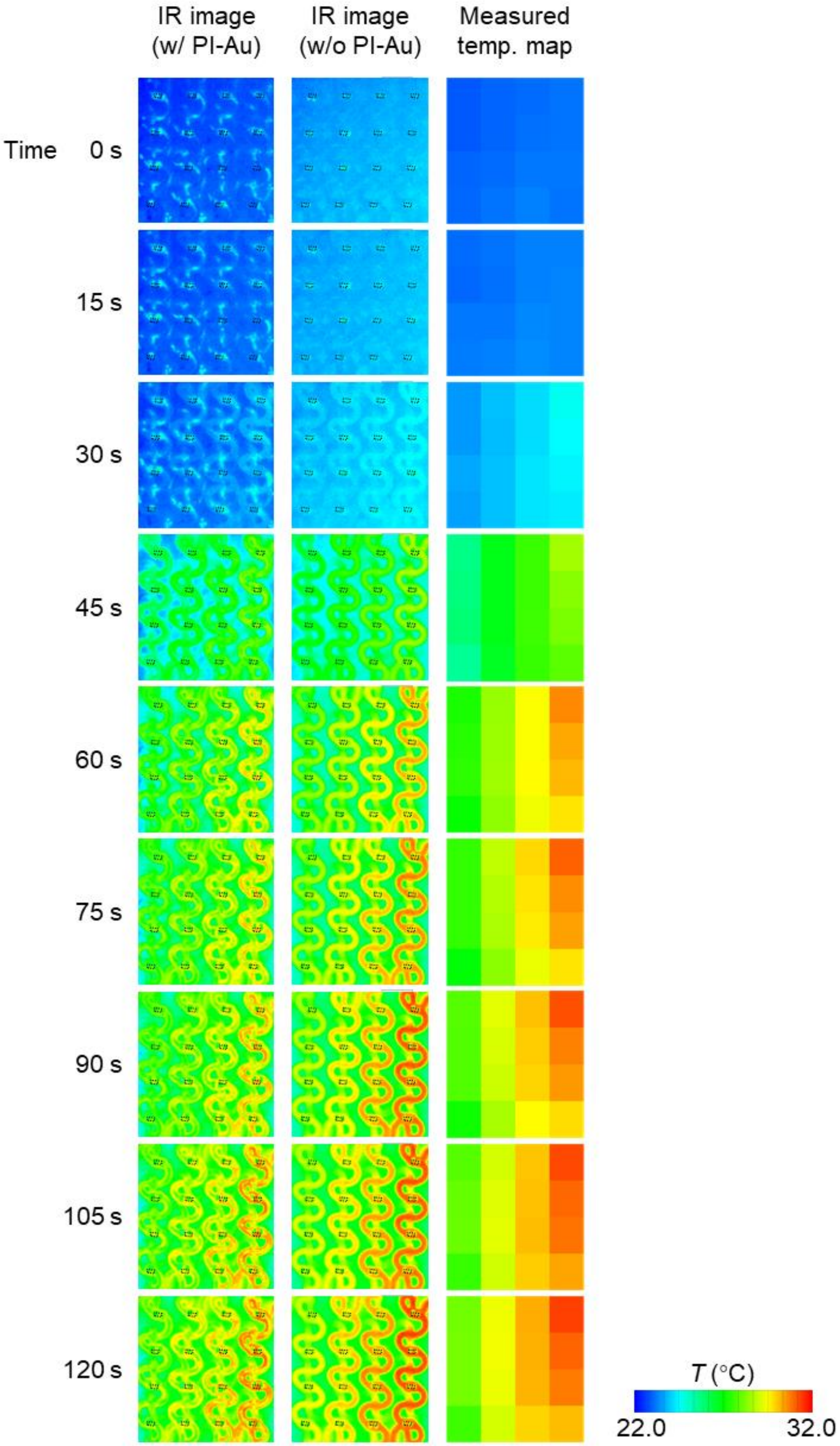

Fig. S40. Comparison of infrared thermal images and measured temperature map of the 3D hybrid system during injection of hot water. This shows the same result as movie S6.

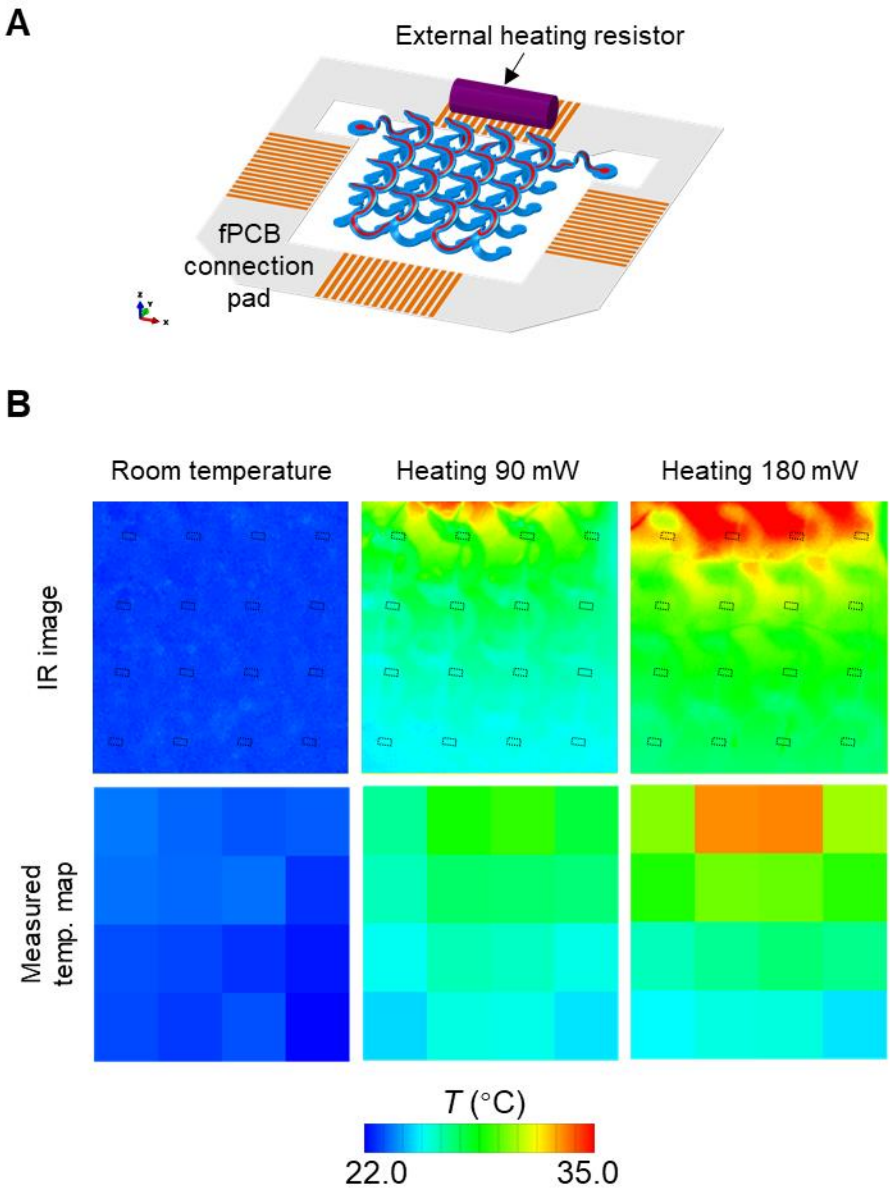

Fig. S41. Comparison of infrared thermal images and measured temperature map of the 3D hybrid system during operation of an external heater. (A) Schematic of device setup. (B) IR images vs measured temperature map.